Marina Brinek, BSc

Sodium Insertion into Spinel-type Lithium Titanium Oxide: Correlation between Crystallinity and Electrochemical Properties

MASTER'S THESIS

to achieve the university degree of

Diplom-Ingenieurin

Master's degree program: Technical Chemistry

submitted to

Graz University of Technology

Supervisors:

Univ.-Prof. Dr. rer. nat. habil. Martin Wilkening

Dr. Ilie Hanzu

Institute for Chemistry and Technology of Materials

Graz, in March 2017

EIDESSTATTLICHE ERKLÄRUNG / AFFIDAVIT

Ich erkläre an Eides statt, dass ich die vorliegende Arbeit selbstständig verfasst, andere als die angegebenen Quellen/Hilfsmittel nicht benutzt, und die den benutzten Quellen wörtlich und inhaltlich entnommenen Stellen als solche kenntlich gemacht habe. Das in TUGRAZonline hochgeladene Textdokument ist mit der vorliegenden Masterarbeit identisch.

I declare that I have authored this thesis independently, that I have not used other than the declared sources/resources, and that I have explicitly indicated all material which has been quoted either literally or by content from the sources used. The text document uploaded to TUGRAZonline is identical to the present master's thesis.

Datum / Date	Unterschrift / Signature

Abstract

Sodium ion batteries are gaining more and more importance as sodium is known for its low cost and high natural abundance, which is beneficial for large scale energy storage technologies. Hence, investigations on new or already existing electrode materials are inevitable in order to further enhance their electrochemical performances.

This work deals with different sample preparations for lithium titanate ($Li_4Ti_5O_{12}$), which serves as an anode material, and their influence on the electrochemical properties. Therefore, three milling methods were explored, dry milling, milling with ethanol (EtOH) or with H_2O and the addition of a surfactant. Each method was performed with different milling durations from 0 min up to 240 min. From the cyclic voltammetry experiments an average sodium storage potential of 0.92 V was determined. Additionally, it turned out, that among all methods, the milling with solvent was most efficient as it features a capacity increase when raising the milling time. This correlates with the galvanostatic cycling studies, which additionally demonstrate specific capacities up to 125 mAh g^{-1}. Furthermore, the average sodium chemical diffusion coefficient, which was found to be in the order of 10^{-20} cm^2s^{-1} by GITT-measurements and NMR-experiments, showed that the ion resides only one specific crystal position, which is assumed to be the octahedral 16c site. Finally, the sodium intercalation mechanism was investigated by *ex-situ* XRD. It seems that a new phase (or phases) is appearing at an insertion potential of about 0.4 V. Unfortunately, the corresponding X-ray reflections could not be identified so far and would need further research.

Kurzfassung

Natrium Ionen Batterien gewinnen zunehmend an Bedeutung, da Natrium für seine niedrigen Kosten und seinem großen natürlichen Vorkommen bekannt ist, was vorteilhaft für großtechnischen Energiespeichertechnologien ist. Folglich sind Untersuchungen an neuen oder bereits existierenden Elektrodenmaterialien unumgänglich, um ihre elektrochemische Leistung weiter zu verbessern.

Diese Arbeit befasst sich mit verschiedenen Probenvorbereitungen für Lithium Titanate ($Li_4Ti_5O_{12}$), welches als Anodenmaterial dient, und dem Einfluss auf die elektrochemischen Eigenschaften. Deshalb wurden drei Mahlmethoden untersucht, trocken gemahlen, mit EtOH oder mit H_2O gemahlen und mit dem Zusatz eines Tensides. Jede Methode wurde mit verschiedenen Mahldauern von 0 min bis zu 240 min durchgeführt. Aus den cyclovoltammetrischen Experimenten konnte ein durchschnittliches Natrium Einlagerungspotential von 0.9 V ermittelt werden. Zusätzlich hat sich herausgestellt, dass unter allen Methoden, jene, die mit Lösungsmittel gemahlen wurden, am effizientesten waren, da sie einen Anstieg der Kapazitäten mit höherer Mahldauer aufwiesen. Dies korreliert mit den Untersuchungen der galvanostatischen Zyklisierung, welche zusätzlich spezifische Kapazitäten bis zu 125 $mAh\,g^{-1}$ aufwiesen. Weiters, konnte mittels GITT – Messungen ein durchschnittlicher chemischer Diffusionskoeffizient für Natrium von ungefähr 10^{-20} cm^2s^{-1} festgestellt werden und die NMR – Experimente zeigten, dass sich das Ion nur auf einer bestimmten Kristallposition aufhält, bei dieser es sich um die oktaedrische Kristallposition 16c handeln dürfte. Schließlich, wurde auch der Interkalationsmechanismus von Natrium mittels *ex-situ* XRD untersucht. Dabei scheint es, als ob eine neue Phase (oder Phasen) bei einem Insertionspotential von etwa 0.4 V auftaucht. Leider konnten die entsprechenden Reflexe noch nicht identifiziert werden, weshalb es weiterer Untersuchungen bedarf.

Acknowledgement

First, I would like to thank my supervisors Univ.-Prof. Dr. rer. nat. habil. Martin Wilkening and Dr. Ilie Hanzu of the Institute for Chemistry and Technology of Materials at Graz University of Technology for their help and input to this thesis. Furthermore, I would like to acknowledge the Christian-Doppler Laboratory for Lithium-Ion Batteries for the financial support.

I would also like to thank every single person of the working group of Prof. Wilkening. Especially Denise Prutsch for her energetic support and the SEM images, Patrick Posch for his continuous advice and, of course, Sarah Lunghammer for the NMR measurements and her valuable comments to this topic. Additionally, I want to acknowledge Dipl.-Ing. Dr. techn. Brigitte Bitschnau and Ao. Univ.-Prof. Dipl.-Ing. Dr. techn. Franz-Andreas Mautner for the X-ray measurements.

Finally, I would like to express my profound gratitude to my parents, siblings and of course to my fiancé Thomas for providing me with tireless support and encouragement during my years of study. Thank you.

Content

List of Abbreviations

CE	Counter electrode
CV	Cyclic Voltammetry
DMC	Dimethyl Carbonate
DSC	Differential Scanning Calorimetry
EC	Ethylene Carbonate
EV	Electrical Vehicle
FEC	Fluoroethylene Carbonate
FWHM	Full Width at Half Maximum
GCPL	Galvanostatic Cycling with Potential Limitation
GITT	Galvanostatic Intermittent Titration Technique
HC	Hard Carbon
LIB	Lithium-Ion Battery
LTO	Lithium Titanate, $Li_4Ti_5O_{12}$
NASICON	Na^+ superionic conductor
NHE	Normal hydrogen electrode
NIB	Sodium-Ion Battery
PC	Propylene Carbonate
RE	Reference electrode
SEI	Solid Electrolyte Interface
TGA	Thermogravimetric Analysis
TMO	Transition Metal Oxide
WE	Working electrode
XRD	X-ray Diffraction

1 Introduction

1.1 Sodium-Ion Batteries

Since the first commercialization of Lithium Ion Batteries (LIB) in 1991, this revolutionary technology has dominated the market of power supply devices.[1,2] Nowadays they are integrated in nearly every imaginable portable electronic device, such as video cameras, mobile phones or notebook computers.[1] One of the main reason why LIBs are such good energy storage systems is, that they possess a high energy density which originates from a very low standard potential of the Li^+/Li redox couple and the small relative atomic mass of Lithium (6.94 g mol^{-1}).[3]
LIBs have been also proved to be promising in larger scale such as alternative power sources for electrical vehicles (EV) or stationary energy storage systems for the integration into the electrical grid.[3,4] However, the application of LIB systems to large-scale storage will be a challenge due to the growing demand and the geographically-constrained Li resources which lead to an increase of the market price of lithium.[4] Although there is a possibility to recycle the metal, the almost endless needs on LIB simply cannot be securely satisfied with the amount of Li mineral reserves. Hence, alternative battery chemistries to that of LIB have to be suggested.[4,5]

Based on already commercialized battery technologies like Na/S and $Na/NiCl_2$ technologies which provide high energy densities, high efficiencies and long cycle lives, a sodium-based battery system could be such a promising alternative to LIB and further investigations on them would be meaningful.[3,4]
Sodium, in contrast to lithium, seems to be inexhaustible due to its high relative abundance and the wide availability of its minerals.[3] For instance, Slater et al stated that 23 billion tons of sodium-containing precursors (soda ash) are located in the United States alone.[4] Additionally, the low costs of sodium salt makes it superior for meeting demand for large scale applications.[2,4]
As sodium, can be directly found below lithium in the periodic table it is the second-lightest alkali metal next to lithium.[3] Furthermore the Na^+/Na redox couple exhibits a standard potential of -2.71 V versus normal hydrogen electrode (NHE), which is a little bit less reducing than that of Li^+/Li (-3.0 V versus NHE).[2] Unfortunately, the 300 mV higher standard reduction potential in combination with the higher atomic mass of sodium results in a lower energy density.[3,4] This lack of energy density can be compensated by utilizing high capacity electrodes or by tuning the voltage difference between cathode and anode to a maximum. In combination with the low

cost advantage of the almost infinite sodium-mineral precursors, NIB may be able to compete with LIB on some sectors, for instance for stationary applications.[2,4]

Another hurdle to overcome is the ability of the intercalation host to accommodate the 0.3 Å larger sodium-ion. Thus, anodes should be employed which provide both, large-enough channels as well as interstitial sites.[4] The larger ionic radii of sodium (1.06 Å) is, however, found not necessarily to be a drawback, due to its accompanying weak solvation energy in aprotic polar electrolytes.[3] Since lithium is a relatively strong Lewis acid which exhibits a high charge density, it has a higher desolvation energy compared to the larger sodium, which has to be overcome for a successful ion diffusion at the electrolyte interface. Hence, a lower desolvation energy results in better kinetics, which in turn improves the battery performance.[3] Although several obstacles still remain, sodium-ion batteries have the potential to be proposed as an alternative technology to conventional Li-ion battery systems.

1.1.1 Setup of a Sodium Ion Battery

The major components of a Sodium-Ion Battery are both insertion materials, cathode and anode, and an electrolyte which separates them.

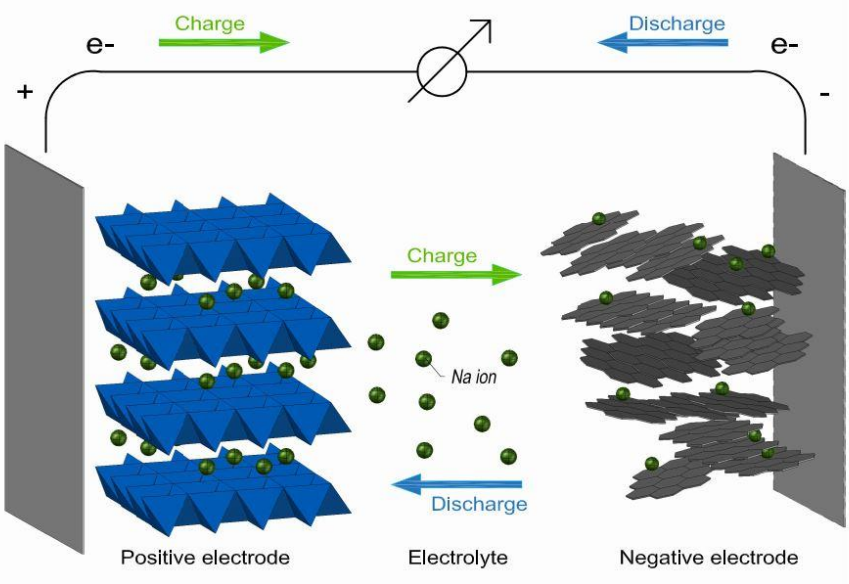

Figure 1: Illustration of the working principle of a Sodium-Ion Battery drawn by Sandra Brinek.

As illustrated in Figure 1 the working principle of NIBs is similar to that of LIBs. Hence, during the battery charging process, Na^+ ions, provided by the cathode are transported through the

electrolyte towards the anode, where they are accommodated. Simultaneously, electrons, which are generated by the oxidation process of the cathode, moves along an external circuit to the anode, since the direct pathway through the electrolyte is hindered by an electronic insulating separator. When the battery is discharged, the process goes the other way around.[6]

1.1.2 Anode Materials

Based on its low melting point (98 °C) and high reactivity with many electrolytes, using metallic sodium induces safety concerns and has to be substituted by appropriate electrode materials. The identification of such an anode material for sodium-ion battery systems turns out to be a significant challenge. An applicable negative electrode should be able to reversibly accommodate Na-ions at voltages at least lower than 2 V and reasonably larger than 0 V (vs. Na^+/Na) to avoid sodium metal plating.[4,5,7]

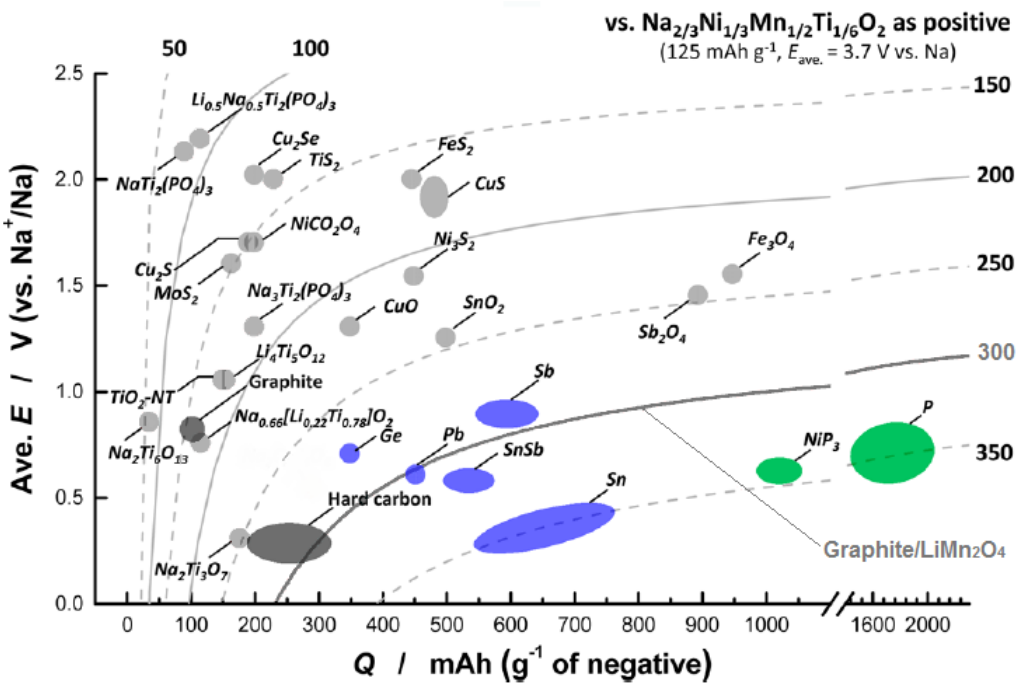

Figure 2: Average Potential and energy density (Wh kg^{-1}) of several proposed negative electrode materials plotted against the specific capacities of already investigated anode materials for NIBs. These anode materials are categorized in carbon-based (black dots) and intermetallic anode materials (blue dots), metal-oxides, sulfides and phosphates (gray dots) and additionally phosphide and phosphorus (green dots).[3]

1.1.2.1 Carbon-based Anode Materials

Graphite is a widely utilized and the most common intercalation host for LIBs as it demonstrates a considerably high reversible capacity (> 360 mAh g^{-1}).[3–5,8] Unfortunately, graphite electrodes are inappropriate for the application in NIBs due to the very limited number of Na ions which can be inserted into the material as well as the electrochemical irreversibility.[3–5]

Although, other carbonaceous materials, such as petroleum cokes, carbon black or pitch-based carbon fibers, have been investigated and proved to intercalate sodium, only hard carbon (HC) won acceptance as anode material of choice for NIB.[4] This non-graphitic, but graphene-containing compound delivers both, a high reversible capacity of almost 300 mAh g^{-1} [3] and a good cyclability.[4,7] Though, it suffers from its low sodium insertion potential (< 0.1 V vs. Na^+/Na), resulting sometimes in metal plating and dendritic formation, which in turn causes safety issues.[7,9]

1.1.2.2 Intermetallic Anode Materials

So far, only a small number of alloy materials are applicable to rechargeable sodium-ion batteries due to their early stage of research.[10]

Investigation of Sn- and Sb-based alloy anodes has gained interest based on their already existing performance in LIBs. During sodiation, both elements form binary alloys with the alkali metal which occurs stepwise. Tin, for instance, reaches a fully insertion phase of $Na_{15}Sn_4$ which is unfortunately accompanied with an inevitable volume expansion of more than 400 %. Antimony, however, has more space to incorporate sodium and hence leads to a lower change in volume.[3,4,10] Furthermore Na-Sb binary systems show high reversible capacities of about 600 mAh g^{-1} and good cyclabilities which even exceed those of the Li-analogous.[10]

Recently, also SnSb/C-nanocomposites were demonstrated to be a promising anode material for NIBs. Due to its good cycle performance and high specific capacity (~ 544 mAh g^{-1}), SnSb/C-composites have the potential to compete with Li-analogous systems.[3,4,10]

1.1.2.3 Metal-Oxides and Other Anode Materials

Since the Sodium insertion potential of many transition metal oxides (TMO) is too high for the utilization in NIBs, the number of those metal compounds, which serves as an appropriate anode material, is limited.[4] Among all oxide electrodes, sodium titanate $Na_2Ti_3O_7$ features the lowest insertion potential (0.3 V) which has been reported for NIBs so far and hence gives rise to an increased energy density.[3–5] However, this anode material has a rather poor cycle life which makes it unsuitable for practical use.[2]

Generally, titanium-based oxides are known for their relatively low price, non-toxicity and their reasonably low redox potential, respectively.[10] The same applies for amorphous TiO_2 nanotubes which additionally demonstrate a reasonably high reversible capacity of 150 mAh g^{-1}. These electrodes provide channels which are large enough (> 80 nm) to transport sodium ions through the liquid electrolyte.[4,8,10]

Beside metal oxides, there are also other types of anode materials which are mentionable, such as sulfide or phosphate-based compounds. Pyrite (FeS_2) and $NaTi_2(PO_4)_3$ are representatives of each type, but unfortunately not for practical use as they suffer on either a bad reversibility or a low capacity.[3,10]

1.1.3 Cathode Materials

In contrast to the limited number of viable anode materials for NIB, the selection of proper cathode materials is vast.[7] To meet the major requirements for such positive electrode materials, the compound should provide both, a reversible Na-insertion at potentials larger than 2 V (vs. Na^+/Na) and a volume change during the intercalation and deintercalation which is almost negligible.[4]

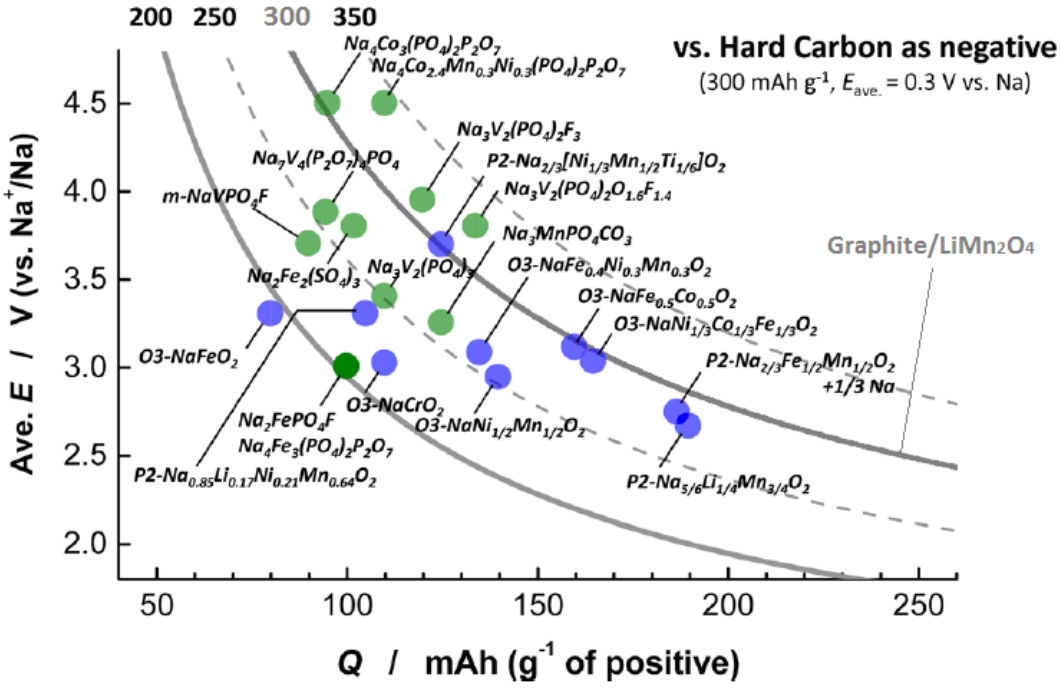

Figure 3: Average Potential and energy density (Wh kg^{-1}) of several positive electrode materials plotted against the specific capacities of already investigated cathode materials for NIBs. These cathode materials are categorized in layered oxides (blue dots) as well as in polyanionic compounds (green dots).[3]

1.1.3.1 Layered Oxide Materials

Since $LiMO_2$ (M= 3d transition metal) is an attractive cathode material for LIBs, it is no surprise that the Na-analogous compound has also been pursued as a suitable electrode material for NIBs.[3,5] $NaMO_2$ structures generally consist of two-dimensional layers of MO_6-octahedras whereas sodium can reside either octahedral (O_n-type) or trigonal prismatic sites (P_n-type) in between.[3,5,8] Although, a phase transformation from P_n to O_n can readily occur by moving the MO_6-layers, the transformation from P_n to O_m, whereas $n \neq m$, is not feasible without bond cleavage of M-O.[3,5]

Na_xCoO_2, for instance, is the Na-counterpart of the already commercialized and most commonly used cathode material for LIBs, namely $LiCoO_2$. For this material three different types (O3-, P3-, and P2-type Na_xCoO_2) are existing, which feature reasonably high reversible capacities of 140, 130 and 120 mAh g^{-1}, respectively.[3,8]

Na_xFeO_2 structures also seem to be promising positive electrode materials for NIBs due to the low cost as well as the non-toxicity of iron-based materials. Although Na_xFeO_2 itself demonstrates bad performance, due to the highly unstable Fe^{4+}, its manganese doped analogue P2-type $Na_x[Fe_{1/2}Mn_{1/2}]O_2$ delivers a reversible capacity of 190 mAh g^{-1} with an operating voltage of 2.5 V. This improvement is explainable by the fact that the new structure stabilizes Fe^{4+}.[3,4,10]

Beside other single transition metal structures such as Na_xMnO_2 [3–5,8] and Na_xCrO_2 [3–5], various transition metal mixtures have also been extensively examined as can be seen in Figure 3.

1.1.3.2 Phosphate-based Materials

Inspired by the phosphate compound $LiFePO_4$ which is a well-known electrode for LIBs, numerous other phosphorous-based materials were investigated.[5,10] These compounds benefits from its high redox potential which results from inductive effects of PO_4^{3-}.[3,10,11] Based on this knowledge, research on cathode materials for NIBs starts to focus on olivine – and NASICON structures.[3–5,8,11]

For instance, Olivine $NaFePO_4$ is a material which is amenable to sodium insertion by achieving a theoretical specific capacity of 154 mAh g^{-1}, though its synthesis is not without difficulties. There is indeed a naturally stable $NaFePO_4$-structure (maricite) existing, but unfortunately it is electrochemical inactive due to the hindered Na-ion migration within the structure.[10,11]

NASICON-compounds have the common structure $Na_nM_2(XO_4)_3$ (X= Si^{4+}, $P^{5+,}$ S^{6+} etc.), which allow Na-ions to reside either spaces between layers or interstitial sites.[8,11] Particularly, $Na_3V_2(PO_4)_3$ has been pursued as a promising alternative to the already existing cathode materials, since it exhibits two plateaus at 1.5 V [11] and 2.6 V [11], which makes it usable as both, cathode and anode.[3,5,11]

Recently, also sodium fluorophosphates such as Na_2FePO_4F, $Na_3V_2(PO_4)_2F_3$ and $NaVPO_4F$, gained interest, as they generally contribute high operating voltages.[3,11]

1.1.4 Electrolyte

Beside electrode materials, it is also plausible to focus research on electrolyte systems, as it has a tremendous impact on the energy density as well as the cycle life of a battery system.[3,12]
The influence on the energy density, for instance, is explained by the electrochemical window of the electrolyte which in turn limits the potential difference of the electrodes.[12,13] In contrast the cycle performance can be improved by the addition of specific additives such as fluoroethylene carbonate (FEC) which is able to build up a passivating film.[4,12,13] Unfortunately, instead of forming a protecting solid electrolyte interphase (SEI), as in the case of lithium, metallic sodium anodes are much rather prone to corrosion.[4] Beside film-forming properties, some additives were also employed due to their resistance against electrode dry-out or their ability to lower the flammability of organic electrolytes, particularly.[3,12]
The electrolyte salt as well as the solvent itself are also components which affect the electrolyte properties to some degree which in turn makes it possible to tune them to be most beneficial.[12] Nevertheless, the components also influence each other which makes it very hard to find an appropriate electrolyte formation.[11] Furthermore, proper electrolyte systems need to be ionic conductive (>1 mS cm^{-1}) but electronically insulating and in addition they should be chemically unreactive against other cell components.[12]
Although, several electrolyte formations have been developed, investigations are still in progress. In the case of NIBs the choice of prospective sodium salts ($NaClO_4$, $NaPF_6$, $Na[N(CF_3SO_2)_2]$, etc.) is limited compared to the number of proper solvents or additives which, however, delivers a variety of electrolyte combinations.[12] Particularly, aprotic polar solvents have been found to form the most appropriate electrolyte compositions.[3,4]
According to Palacin et al., who examined various different electrolyte formation for NIBs, $NaClO_4$ combined with in propylene carbonate (PC) or ethylene carbonate (EC) demonstrated the best cyclability when using hard carbon as an electrode.[3]

1.2 Lithium titanate $Li_4Ti_5O_{12}$

Since both alkali metals, lithium and sodium, share many similar chemical and physical properties, it is not surprising that a way to find appropriate electrode materials for NIBs is by starting with Li-intercalation structures and their Na-analogues.[5,10]

Lithium titanate, $Li_4Ti_5O_{12}$ (LTO) is such a promising electrode material as it has the potential to compete, on some sectors, with graphite, the most commonly used anode material in LIBs.[14,15] Due to its 1.55 V higher Li-insertion potential compared to Graphite (0 V vs. Li^+/Li), LTO is not prone to dendrite formation, which in turn prevents short circuits.[14–16] Furthermore it demonstrates a reasonably high capacity retention, resulting from a readily occurring Li-insertion and deinsertion which paves the way for long life stationary applications. The spinel – type anode material also benefits from its minimal volume change during the Li-intercalation process, making LTO a zero-strain material.[7,14,15]

As can be seen in Figure 4 lithium titanate, $Li_4Ti_5O_{12}$, originally bears lithium ions on octahedral 16d as well as on tetrahedral 8a site (Li^{8a}) when x = 0. During lithiation, additional Li^+ ions which are inserted move to the octahedral 16c sites while Li^+ ions which initially occupy 8a sites also start to reside on 16c sites until LTO is fully inserted. This leads to a dense and compact rock – salt structure ($Li_7Ti_5O_{12}$) where all 16c sites are filled, the formerly occupied 8a sites are empty and the Li-ions which originally resides the 16d octahedral sites remain unchanged.[14,15]

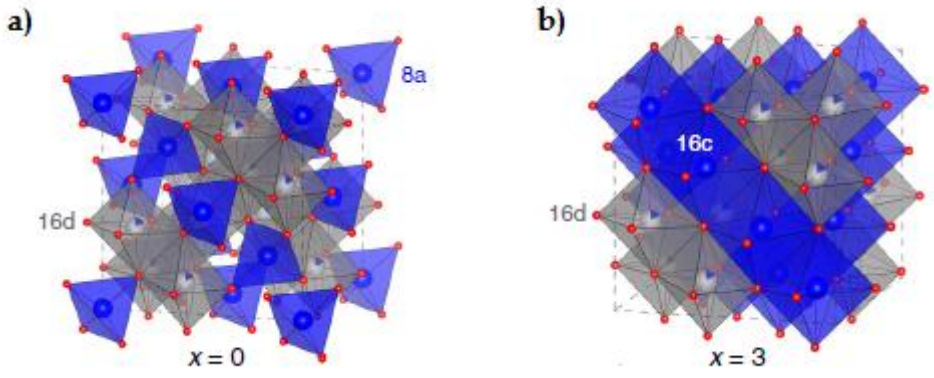

Figure 4: Crystal structures of **a)** $Li_4Ti_5O_{12}$, the pristine sample, and **b)** $Li_7Ti_5O_{12}$, which is fully inserted with Lithium[14]

Zhao Liang et al. reported for the first time, that LTO can be employed as an anode material for both, LIBs as well as NIBs. It is noteworthy, that this spinel-type structure has the ability to

bear both ions, Li^+ and Na^+, while demonstrating a reversible capacity of 145 mAh g^{-1}.[2] Supplementary studies of Sun et al. match the preliminary investigations of Liang et al. while they additionally came up with a possible sodium insertion mechanism, calculated via DFT. According to this mechanism, sodium ions initially start to reside the octahedral 16c sites, rather than the 8a tetrahedral sites, due to their sizes. Additionally, analogous to the Li-insertion process, Li^{8a} also moves to the octahedral 16c sites, giving rise to a phase separation of $Li_7Ti_5O_{12}$ and $Na_6LiTi_5O_{12}$. Hence, Sun et al. proposed the following three-phase separation mechanism:[7]

$$2\,Li_4Ti_5O_{12} + 6\,Na^+ + 6\,e^- \rightleftharpoons\ Li_7Ti_5O_{12} + Na_6LiTi_5O_{12} \qquad (1)$$

1.3 Used Methods and Techniques

1.3.1 X-ray Diffraction (XRD)

X-ray Diffraction (XRD) is a multifunctional and non-destructive method to characterize and identify the ordering of ions and molecules in crystalline samples.[17–19]

This method is based on diffraction of a monochromatic X-ray beam, which can be generated in a sealed tube. In this case, an electron beam, coming from a filament cathode, is focused towards a specific anode material that emits a X-ray photon whereas each material or atom has its characteristic radiations (e.g. Cu Kα).[19] When this X-rays hits the crystalline sample, the beam will be scattered by the regular arrangement of its atoms, resulting in constructive (in phase) or destructive (out of phase) overlapping of the incoming X-ray waves.[6,18,19] However, the constructive interference of the light waves is solely responsible for the specific reflections which in total form a diffraction pattern.[6,18] Each pattern is like a fingerprint of the corresponding material, comprising information regarding the size and shape of the crystal lattice as well as the relative position of its atoms.[6]

According to Bragg's law a crystal lattice can be considered as an arrangement of imaginary atomic planes on which the X-rays are reflected. This model can be mathematically expressed by using Equation **(2)**, where d indicates the distance between neighboring planes, θ is the angle of the incident X-ray, n is the order of reflection (normally n=1) and λ is the wavelength.[18–20]

$$2d * sin\theta = n * \lambda \tag{2}$$

Furthermore, the lattice planes can be described by the Millers indices h, k and l, which are the reciprocals of the axes intercepts (x/h, y/k and z/l) as can be seen in Figure 5. Hence, the corresponding d-values d_{hkl} enable conclusion regarding the parameters of a crystal lattice.[18,19]

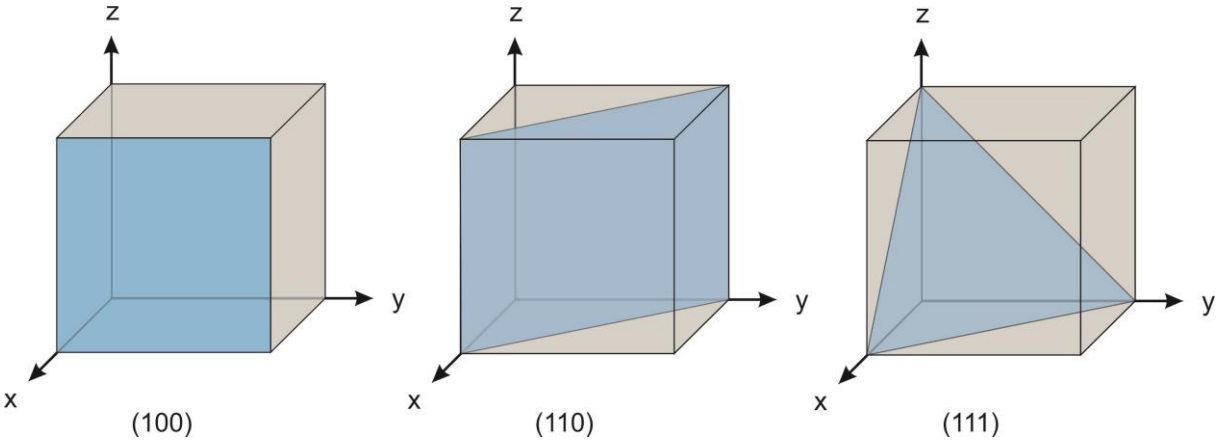

Figure 5: Examples of lattice planes described by the Millers indices.

Another important parameter which can be simply gained by X-ray Diffraction is the average crystallite size of the sample. This information can be determined by using the Scherrer equation **(3)**, where K is a constant which takes the crystal shape into account, β is the full width at half maximum (FWHM) of the reflection and θ is the diffraction angle.[17,19,20]

$$L = \frac{K\lambda}{\beta * cos\theta} \tag{3}$$

As a result, a decreasing crystallite size is directly related to a reflection broadening in the X-ray diffractogram. However, the reflection broadness should be handled with caution as it can be also influenced by micro-strain effects.[19]

1.3.2 Cyclic Voltammetry

Cyclic Voltammetry (CV) is almost always the first technique of choice to retrieve initial information about electrochemical reactions. Particularly, CV is used to examine the reaction mechanism of a redox species, its stability, reversibility or the location of its redox potentials, for instance.[21–23]

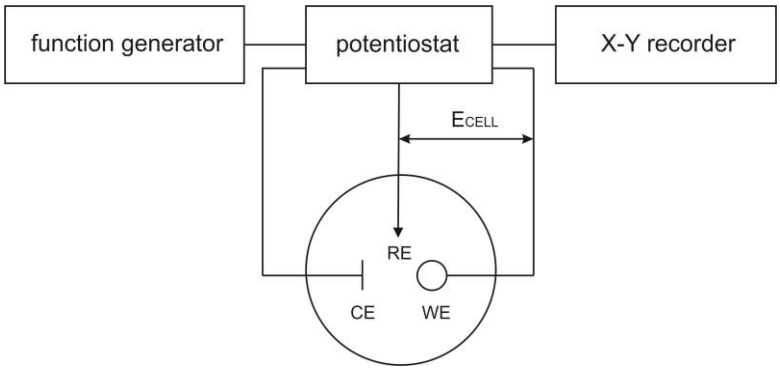

Figure 6: Schematic scheme of the fundamental working principle of cyclic voltammetry by using a three-electrode arrangement

Generally, a cyclic voltammetry experiment is operating with a three-electrode arrangement – the working electrode (WE), counter electrode (CE) and reference electrode (RE), respectively – where the potential of the WE is scanned between two potential limits. A function generator provides this target potential E_{CELL} between the WE and the RE (Figure 6). In galvanostatic mode, if an electrochemical reaction occurs at the electrode interface, the potential between WE and RE changes to E_{ACTUAL}, the potentiostat measures the potential difference ΔE and adjusts a current across the CE and WE to maintain the initial potential difference E_{CELL}. Meanwhile the X-Y recorder gathers data like the applied voltage or the corresponding current response, which can be used to depict cyclic voltammograms.[23,24]

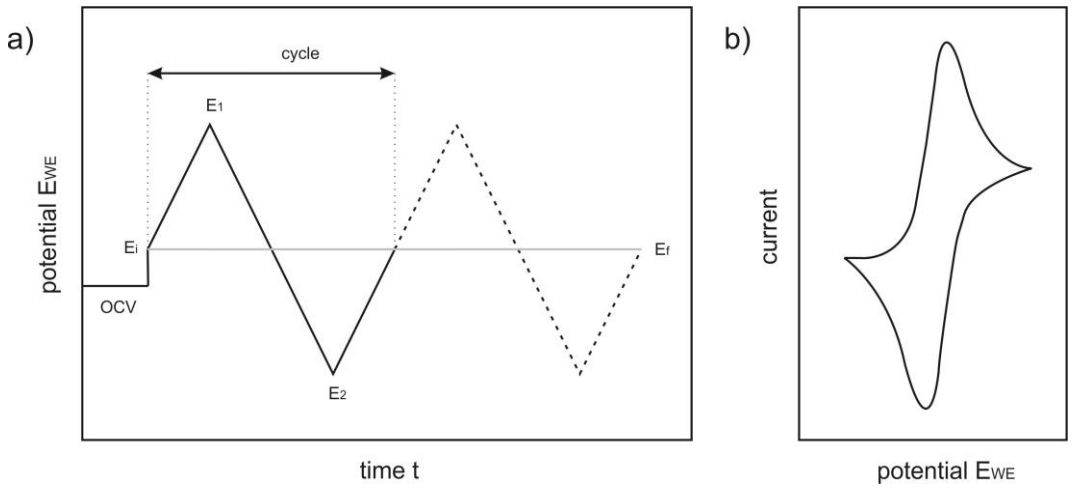

Figure 7: Cyclic Voltammetry operation principle. **a)** Potential applied between the reference and working electrode as a function of time and **b)** the corresponding cyclic voltammogram.

Figure 7 b indicates such a voltage-current behavior with the corresponding triangular potential wave (Figure 7 a). The cyclic voltammogram of simple reversible electrochemical reaction usually consists of both a reduction and an oxidation peak, respectively. In the particular case of a highly reversible one-electron transfer reaction, the distance between both peaks is 59 mV at ambient conditions. However, beside the potential separation, there are also other characteristics such as shape, position or number of peaks, which delivers useful information regarding the electrochemical aspects of the reaction.[25]

1.3.3 Galvanostatic Cycling with Potential Limitation (GCPL)

Galvanostatic cycling with potential limitation (GCPL) is a type of chronopotentiometry which is commonly used to examine battery systems determining their capacity or cyclability, for instance.[26]

This constant-current technique is mainly executed with a three-electrode set-up, where a specific current is applied to the WE, causing a steep increase of the potential which is measured as a function of time (Figure 8).[23] If an electroactive species is present, it consumes as the imposed current passes and the concentration gradient from the surface to the bulk of the electrode is formed. After a certain time, when the surface concentration of the reactant is zero, the potential further increases to a potential at which the next possible reduction can occur and thus potential limits have to be adjusted to avoid undesired side reaction (e.g. decomposition of the electrolyte). Subsequently, the current is reversed to an equal magnitude, the electroactive species starts to be oxidized and the potential decreases.[22,25,27] If this process is repeated several times, it is denoted as cyclic chronopotentiometry (or galvanostatic cycling) which is depicted in Figure 8 b.[22]

Chronopotentiometry is also a simple tool to quantify the diffusion coefficient by determining the transition time τ at different current densities i_0. This can be readily conducted by using the Sand equation **(4)**, where F is the Faraday constant, C* is the concentration of the Redox species and D its diffusion coefficient.[25,28]

$$\tau^{1/2} = \frac{\pi^{1/2} n F C^* D^{1/2}}{2\, i_0} \qquad (4)$$

However, an accurate measurement of τ is hampered for very short time periods. In this case, there is a major discrepancy between the faradaic and the imposed current, which originates from current sacrificed for charging the double layer.[25]

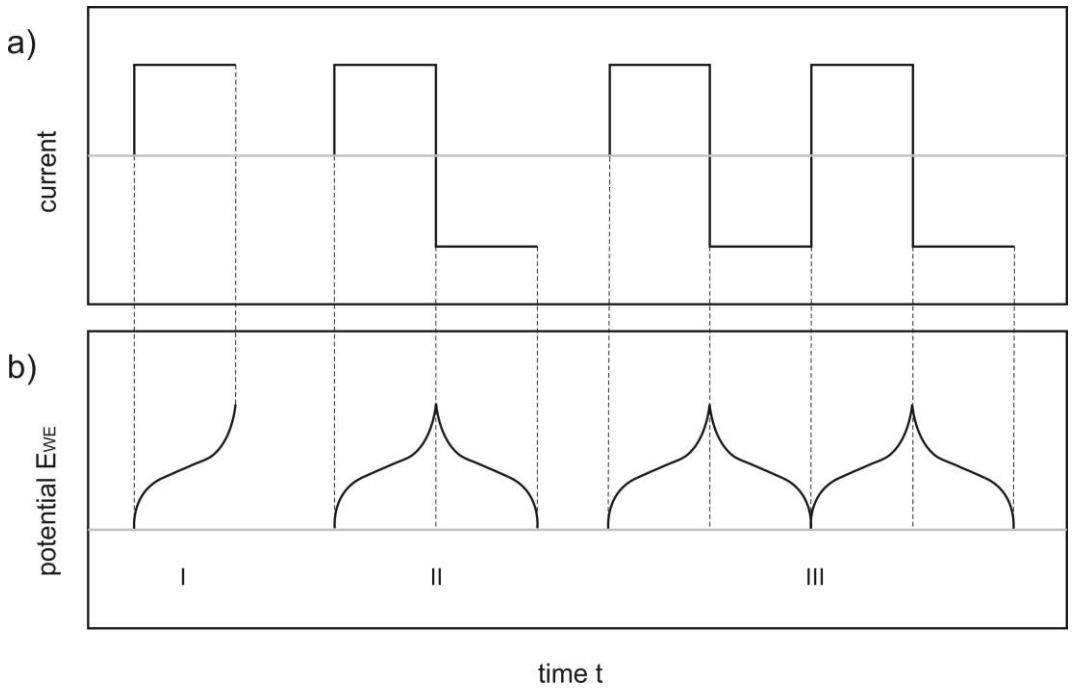

Figure 8: Different types of chronopotentiometric experiments. **a)** the applied current and **b)** the corresponding potential response resulting in a (I) constant current chronopotentiometry, (II) current reversal chronopotentiometry or (III) cyclic chronopotentiometry

1.3.3.1 Galvanostatic Intermittent Titration Technique (GITT)

The galvanostatic intermittent titration technique (GITT) is another type of chronopotentiometry, but less frequently used than galvanostatic cycling. The possibility to gather thermodynamic as well as kinetic parameters, makes it an indispensable tool in battery research.[26,29–31]

GITT is based on the same principle as the previously discussed galvanostatic cycling, except the fact that the constant current is applied, as the name says, intermittent. Therefore, this technique consists of an initial current pulse, which is hold for a specific time period as can be seen in Figure 9 a.[26,30,31] This current pulse is followed by a sequence where no current is applied, so that the system is allowed to relax back to open circuit conditions.[29,31]
When the WE is supplied with a charging current, the potential abruptly starts to either increase or decrease very rapidly, which derives from the iR drop. Afterward, the potential change become smaller as a result of the gradually formed concentration gradient.[26,29] Subsequently, the current is cut off which gives again rise to a large potential change, originating from a drop in iR, and followed by a small change.[29] During the slow potential rate, the ions diffuse towards

the electrode surface to achieve a homogeneous distribution, where dE/dt ≈ 0.[29–31] This process is repeated until the voltage cut-off is reached and the material is fully charged. During the discharging step, the applied current is reversed and the procedure goes in the opposite direction.[29,31]

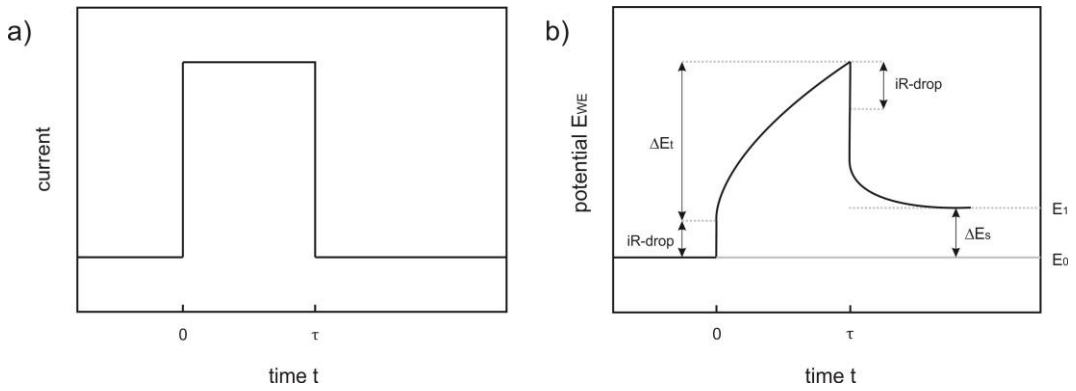

Figure 9: Working Principle of Galvanostatic Intermittent Titration Technique (GITT). **a)** indicates the applied current and **b)** the potential response.

Based on the knowledge that the voltage change is directly related to the chemical diffusion process and the assumption that this diffusion is subjected to Fick's law, the chemical diffusion coefficient can be calculated by using the following equation:

$$D = \frac{4}{\pi}\left(\frac{i\,V_m}{z_A F S}\right)^2 \left[\left(\frac{dE}{d\delta}\right) \Big/ \left(\frac{dE}{d\sqrt{t}}\right)\right]^2 \tag{5}$$

Here, i indicates the applied current, V_m is the molar volume of the electrode material, z_A is the charge of the electroactive species and S is the area of the electrode/electrolyte interface. Additionally, dE/dδ represents the linear correlation between the steady state voltage and its titration step δ and dE/d√t is the dependence of the electrode potential and the square root of the time.[26,29–33] If the imposed currents are considered to be very small, equation **(5)** can be transformed in an even simpler form:

$$D = \frac{4}{\pi\,\tau}\left(\frac{n_m V_m}{S}\right)^2 \left(\frac{\Delta E_s}{\Delta E_t}\right)^2 \tag{6}$$

where τ is the time duration of the current pulse, nm is the number of moles, ΔE_s is the change of the steady-state voltage and ΔE_t the corresponding voltage change during the current pulse, neglecting the iR drop as can be seen in Figure 9 b.[26,29,32]

However, the value of the chemical diffusion coefficient, determined with the above mentioned equations should be treated with caution, as the method does not take phase transformation into account.[33]

2 Experimental procedure

2.1 Methods

The powdered lithium titanate was annealed by using a glass oven B585 from BÜCHI (www.buchi.com, Switzerland) and milled via planetary micro mill Pulverisette 7 premium line from FRITSCH (www.fritsch-international.com, Germany)

The electrode slurries were prepared via planetary micro mill Pulverisette 7 classic line from FRITSCH (www.fritsch-international.com, Germany)

The electrode slurries were casted on copper current collectors with a film Applicator COATMASTER 510 from ERICHSEN (www.erichsen.de, Germany)

The samples were characterized via X-ray diffraction (XRD) using a diffractometer from Bruker D8 Advance (www.bruker.com, USA) with Cu Kα radiation.

Cyclic Voltammetry as well as Galvanostatic Cycling was carried out by using a multichannel VMP-3 and MPG-2 potentiostat from Biologic Science Instruments and an EC-Lab® VIO-34 Software (www.bio-logic.info, France).

The Galvanostatic Intermittent Titration Technique was carried out with the same methods as Cyclic Voltammetry and Galvanostatic Cycling.

SEM-pictures were generated on an INCA X-act PentaFET Precision TESCAN electron microscope from Oxford Instruments (www.oxford-instruments.com, England).

The particle size of the LTO-powder was determined by using a Lasergranulometer CILAS 1180 (www.cilas.com, France).

^{23}Na Magic-Angle-Spinning (MAS) NMR spectra were recorded on a 300 MHz instrument from Bruker (www.bruker.com, USA), by using a Teflon probehead of 11.7 T which results in a resonance frequency of 132 MHz for sodium nuclei.

The data evaluation and the corresponding graphics were performed by using the data analysis software IGOR Pro.

2.2 Material Preparation

Lithium Titanate, $Li_4Ti_5O_{12}$ (LTO) was prepared for electrochemical characterization in three ways. First LTO was dry milled, then it was milled by using absolute EtOH and afterwards it was milled with dest. H_2O and the addition of a Surfactant (Dispex®A40).

Dry milled LTO

Approximately 30 g of LTO were transferred to the BÜCHI and treated with 300°C for 24 hours in vacuum to get rid of possible oxidation products caused by long storage duration. After the annealing process the LTO (within the glass oven) was transferred to the glovebox, in order to avoid any contact with the ambient air. For the subsequent ball milling procedure 6 samples were prepared and treated with different milling times (0, 15, 30, 60, 120 and 240 min). Each milling beaker contained 5 g of the white powdered sample and 180 ZrO_2 balls.

LTO milled with EtOH

LTO was prepared in the same way as the dry milled one apart from the addition of 9 g absolute ethanol in the milling processes.

LTO milled with H_2O and a surfactant

Different to the other methods here the LTO was milled prior to the annealing step, whereas the temperature was increased stepwise to prevent uncontrolled degassing of the sample as can be seen in the TGA in Figure 22 (Appendix, section 6.2). The milling step was prepared in the same way as the dry milled one apart from the addition of 9 g destilled water and a drop of Surfactant.

The working electrodes were prepared by using 1 g of the active material $Li_4Ti_5O_{12}$ (75 wt%), conductive material Super C65 (15 wt%) and binder Kynar 2801 PVdF (10 wt%). In Addition 3 g of the Solvent NMP (1-Methyl-2-pyrrolidinone) were added to allow that the slurry can be casted. After ball milling, the slurries were casted onto a copper foil with a thickness of 100 µm and a casting speed of 5 mm/s. To remove the solvent, the casted slurries were dried in the drying oven at 60°C for only 1 hour to keep the duration of air exposure as short as possible. Subsequently the electrodes were cut out with a diameter of 10 mm and dried under vacuum at 60°C. After weighing, the electrodes were dried for a second time and transferred into the

glovebox. Then the as-prepared electrodes were assembled in Swagelok test-cells for further electrochemical analysis.

2.3 Electrochemical Characterization

As illustrated in Figure 10 the prepared electrodes were assembled in three-electrode Swagelok cells using metallic sodium as both counter- and reference electrode. Both electrodes were assembled with two Separators (Whatman™ GF/B glass microfiber) on each side immersed in 800 µl of a 1 M solution of $NaClO_4$ in propylene carbonate (PC). The entire process was carried out in a glovebox under inert atmosphere.

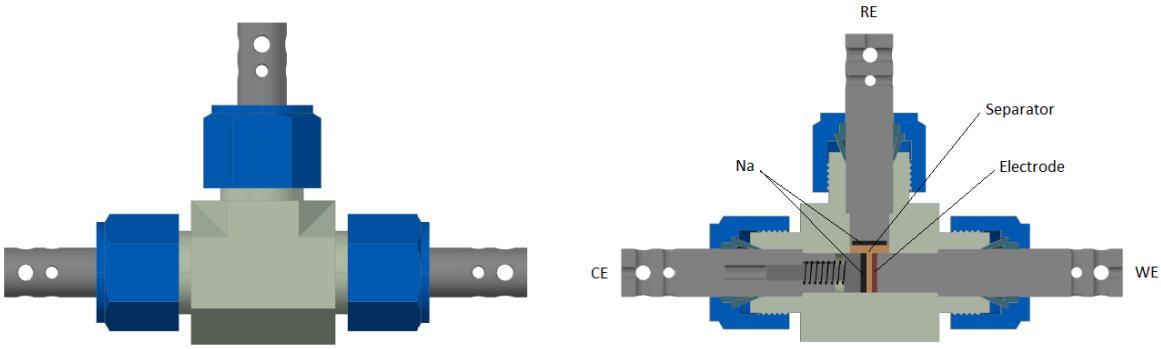

Figure 10: Finally assembled three-electrode Swagelok cell (on the left side) and the cross section of such a cell and the corresponding constituent parts. The reference- (RE), counter electrode (CE) assembled with metallic sodium and separators on each side and the working electrode (WE) assembled with the electrode (on the left). Graphic drawn by Sandra Brinek.

Those Swagelok cells were then used to record cyclic voltammograms and for the constant current experiments.

2.3.1 Methods and Parameters

As mentioned above the cells were electrochemically analyzed by using Cyclic voltammetry (CV), Galvanostatic Cycling with Potential Limitation (GCPL) and Galvanostatic Intermittent Titration Technique (GITT). Each method was performed on either a VMP-3 or MPG-2 potentiostat from Biologic.

For the cyclic voltammetry experiment the cell was first allowed to rest for 12 hours to stabilize the OCV. The initial voltage and the final voltage were set to 0.0 V vs. the OCV value after 12 h and in between the potential of the working electrode was scanned between the two vertex limits 0.1 and 2.8 V vs. reference (Na^+/Na) by using different scan rates of 0.05, 0.1, 0.2, 0.5, 1, 2, 5, 10, 20 and 50 mV/s, respectively. Each scan rate was applied for two cycles.

The cycling studies were performed by using the GCPL-technique (galvanostatic cycling with potential limitation). After a resting time of 12 hours, current steps of 20, 50, 100, 200 and again 20 mA g^{-1} were applied. Each step was hold for 24 cycles resulting in 120 cycles for each cell. The lower potential limit was set a little bit higher as in the cyclic voltammetry experiment, to avoid some electrolyte decomposition. Hence, the cell was cycled in the potential range of 0.2 – 2.8 V.

The GITT-experiment again starts with a resting time of 12 hours which is followed by current pulses, determined via capacities gathered from preceding experiments. Each current pulse was hold for 10 min, followed by a relaxation time of 1 hour, where the current was completely interrupted. The cell was cycled within the same potential range as the GCPL-experiment, but for only two cycles.

2.4 Particle Size Determination

In order to determine the particle size of the different pretreated LTO-powder, a Lasergranulometer from CILAS was employed. Therefore, a small amount of LTO was dissolved in dest. H_2O and the addition of a Surfactant and stirred with an ultrasonic finger for 30 s. Afterwards the solution was pumped through the detection reservoir while it was continuously stirred with the help of an ultrasonic bath.

2.5 NMR-measurement

For this experiment, powdered LTO was pressed into pellets by using a lab press from P/O/WEBER with a pressing force of 78 kN and in an argon-filled glovebox. After the pressing step the pellets were installed in the Swagelok cells in the same way as the casted electrodes as described in section 2.3. For the sodium insertion, the cells were again subjected to a GCPL experiment, whereas only half a cycle was carried out. That means, that after a resting step of 12 hours, only one sequence containing a current rate of C/50 was adjusted to ensure a very

slow sodiation down to 0.2 V. The corresponding capacities which enables the determination of the applied currents were gathered from the galvanostatic cycling experiment.

After the sodium-insertion was completed, the cell was disassembled in the glovebox, to dismount the blue colored pellet. Subsequently, the pellet undergoes several rinsing steps with both, PC (5x) and Dimethyl Carbonate (DMC, 5x), followed by a final drying step at 60°C under vacuum. Afterwards, together with quartz wool, the resulting powder is enclosed in a quartz tube via natural gas burner. Those quartz tubes, were then used to reveal the insertion mechanism of sodium into LTO by using ^{23}Na NMR MAS.

2.6 *Ex-situ* X-Ray Diffraction

In order to investigate the phase transformation of $Li_4Ti_5O_{12}$ during the sodiation, the process was stopped at specific intercalation and deintercalation stages and the resulting samples were characterized via XRD.

Therefore, pellets of the powdered anode material had to be press and embed in a Swagelok cell as described above (section 2.5). The used technique was also similar to the NMR sample preparation, except the fact, that the procedure was interrupted at particular potential as shown in Figure 11 . After the rinsing and drying step, the sample was transferred into a glass capillary for further analysis.

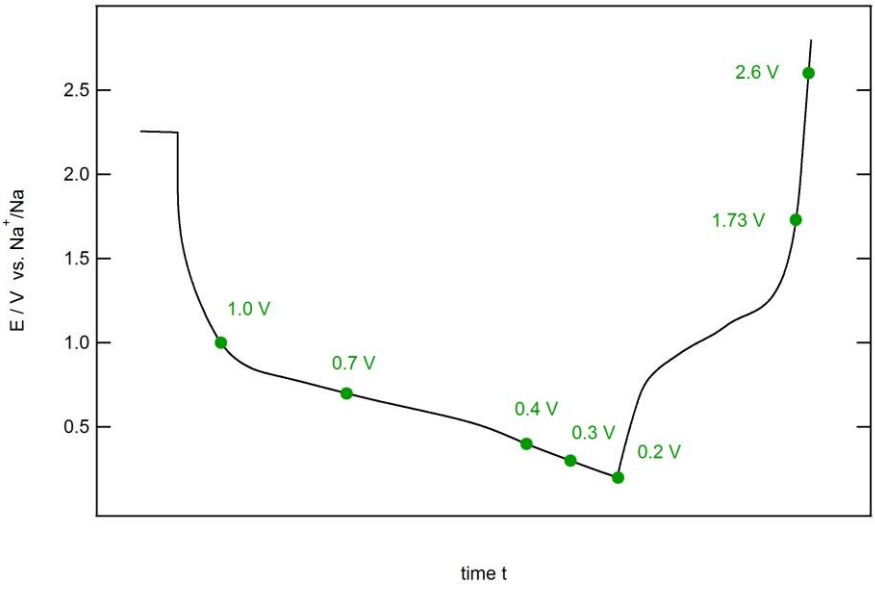

Figure 11: Sodium insertion and deinsertion into LTO stopped at specific potential limits used for phase transformation analysis via *ex-situ* XRD.

3 Results and Discussion

3.1 X-Ray Diffraction

Figure 12 shows the X-ray diffractrogram of lithium titanate pretreated with different milling times and the corresponding reference material, extracted of the ICSD database. The reflections match perfectly with those of the reference, which leads to the fact, that the used LTO did not undergo a phase transformation. Some reflections at higher diffraction angles are only weak identifiable compared to the reference which is due to the background, coming from amorphous parts of the samples. This amorphous nature seems to increase with higher milling time, which is most likely induced by mechanical shear forces which affects the crystallinity of the sample during the milling process. Another effect of a higher milling time was found in the reflection broadening, which is an indication for a reduction of the crystallite size, according the Scherrer equation **(3)** in section 1.3.1.

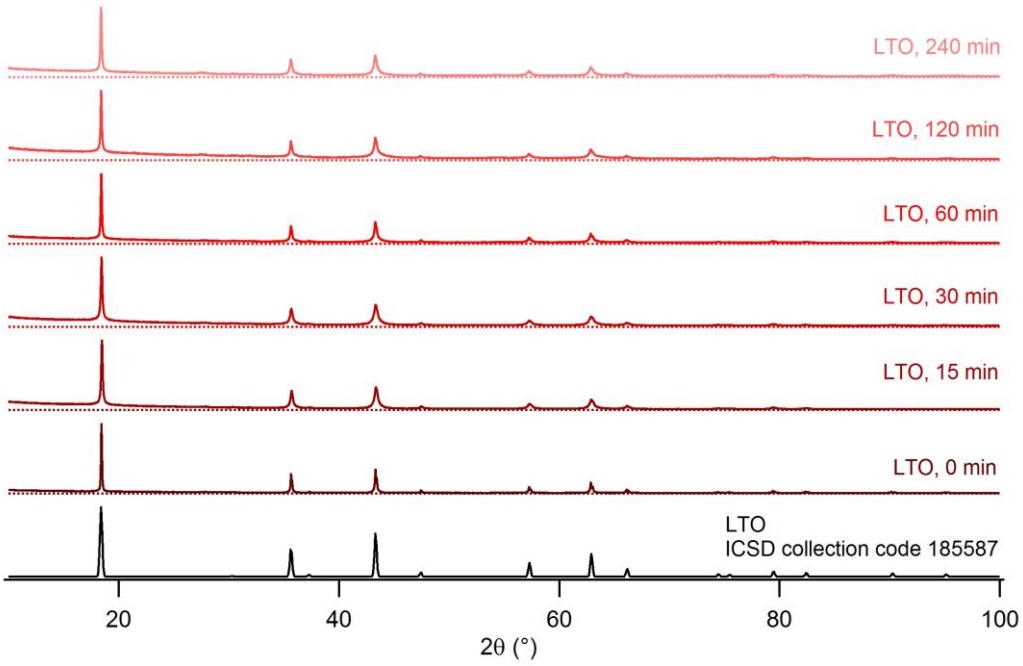

Figure 12: X-ray diffractogram of dry milled LTO at different milling times and the corresponding reference (black).

Beside the dry milled method, lithium titanate was also milled with the addition of a solvent. In the case of the EtOH milled LTO, the X-ray Diffractogram shows similar results as the dry milled LTO (Figure 23, Appendix, section 6.3).

In contrast to the preceding samples, the diffractogram of LTO milled with H_2O and the addition of a surfactant exhibits different results as can be seen in Figure 13. It becomes apparent, that particularly this milling procedure affects the crystallinity of lithium titanate when reaching a milling time of 60 minutes. In particular, four sets of new reflections were detected and denoted with letter A – D, whereas the first set (A) starts to grow at a milling time of 60 min. This phase transformation consists of three reflections at phase angles of about 28°, 30° and 32° as can be seen in the right column of Figure 13. The outer reflections at 2θ = 28° and 23° are additional peaks, which do not refer to the crystalline nature of LTO, whereas the centered reflection (2θ = 30°) belongs to the spinel-structure. The intensity of the entire set of reflections becomes higher with higher milling time. The additional sets of reflections (B – D), are only identifiable in the last three milling steps starting at 240 min, whereas the 12 h and 24 h of milling time were additionally introduced to see, if the effect further increases. Moreover, the higher milling time has again an impact on the crystallite size, indicated by the increasing reflection broadness.

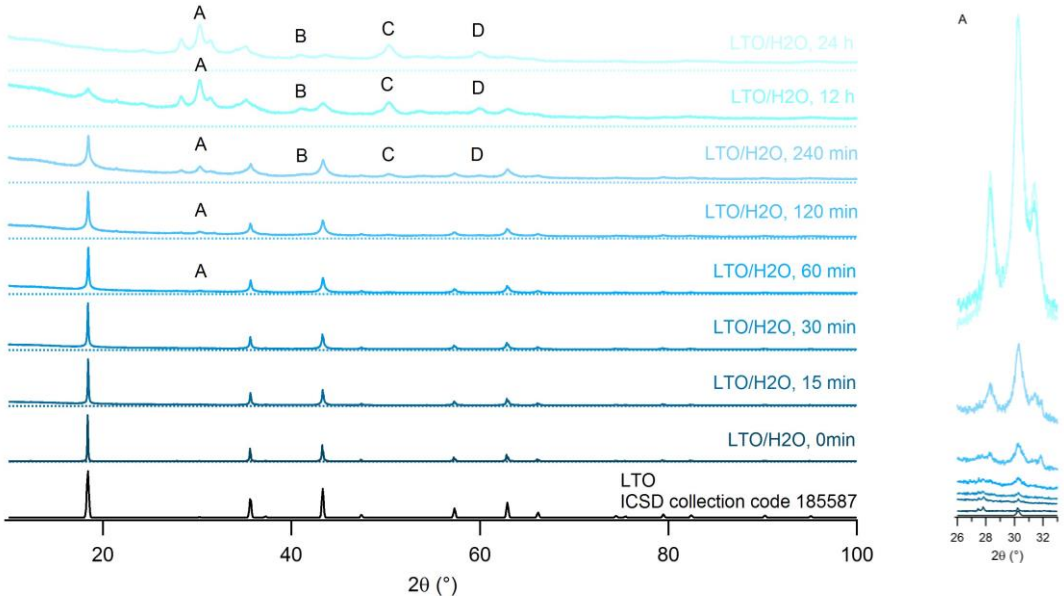

Figure 13: X-ray diffractogram of LTO which was milled with H_2O (and the addition of a surfactant, see text) at different milling times and the corresponding reference (black). The letters A, B, C and D indicate lattice planes, which do not correspond to that of the reference material, whereas region A is highlighted in the right column.

Figure 14 indicates the comparison of the X-ray diffractograms of all three methods (dry milled, or milled with either EtOH or H_2O) milled for 120 min and the corresponding reference material. From the bottom up, it can be seen, that the reflections broaden, which might be again explainable by a decrease in the crystallite size as mentioned above. The reflections match

perfectly with those of the reference, except the additional set of reflections A (defined in Figure 13) of the water-milled LTO. Since they were only weak identifiable, the 120 min milled samples were also chosen for further comparison.

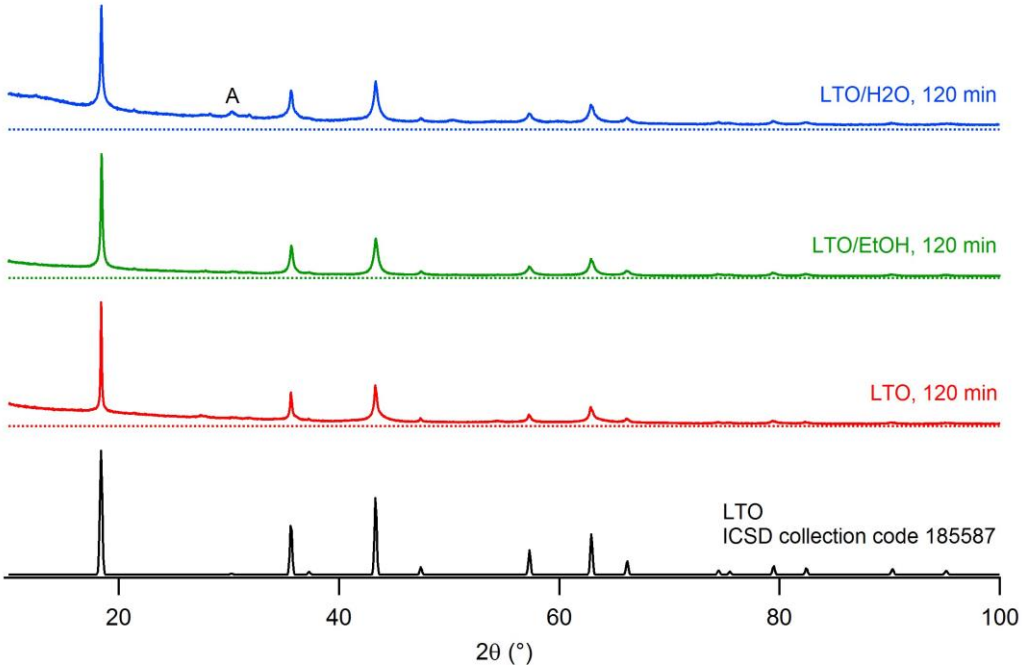

Figure 14: X-ray Diffractogram of LTO which was dry milled (red), milled with EtOH (green) or with H_2O (blue) for 120 min and the corresponding reference (black). Letter A indicates a lattice plane, which do not belong to the reference material

3.2 Morphological Characterization

The morphological characterization was performed by using scanning electron microscopy (SEM) analysis, in order to study the influence of different milling methods and duration on the surface structure of $Li_4Ti_5O_{12}$.

Figure 15 a displays the acquired SEM image of the pristine sample, indicating that the used LTO initially consists of particles which are almost equal sized. The following images Figure 15 b – j show the different sample preparations of lithium titanate, with a milling time of 60 min (2^{nd} row), 120 min (3^{rd} row) and 240 min (4^{th} row). By considering the dry milled method (Figure 15 c, f, i), it becomes apparent, that the initially fine distributed particles arranged themselves to form larger, agglomerate structures, until they finally end up as compact but porous micrometer-sized spheres at a milling time of 240 min.

Following the sample preparation of the EtOH milled lithium titanate in the centered column (Figure 15 c, f, i), an aggregation of the particles can be observed too. In this case, the particles

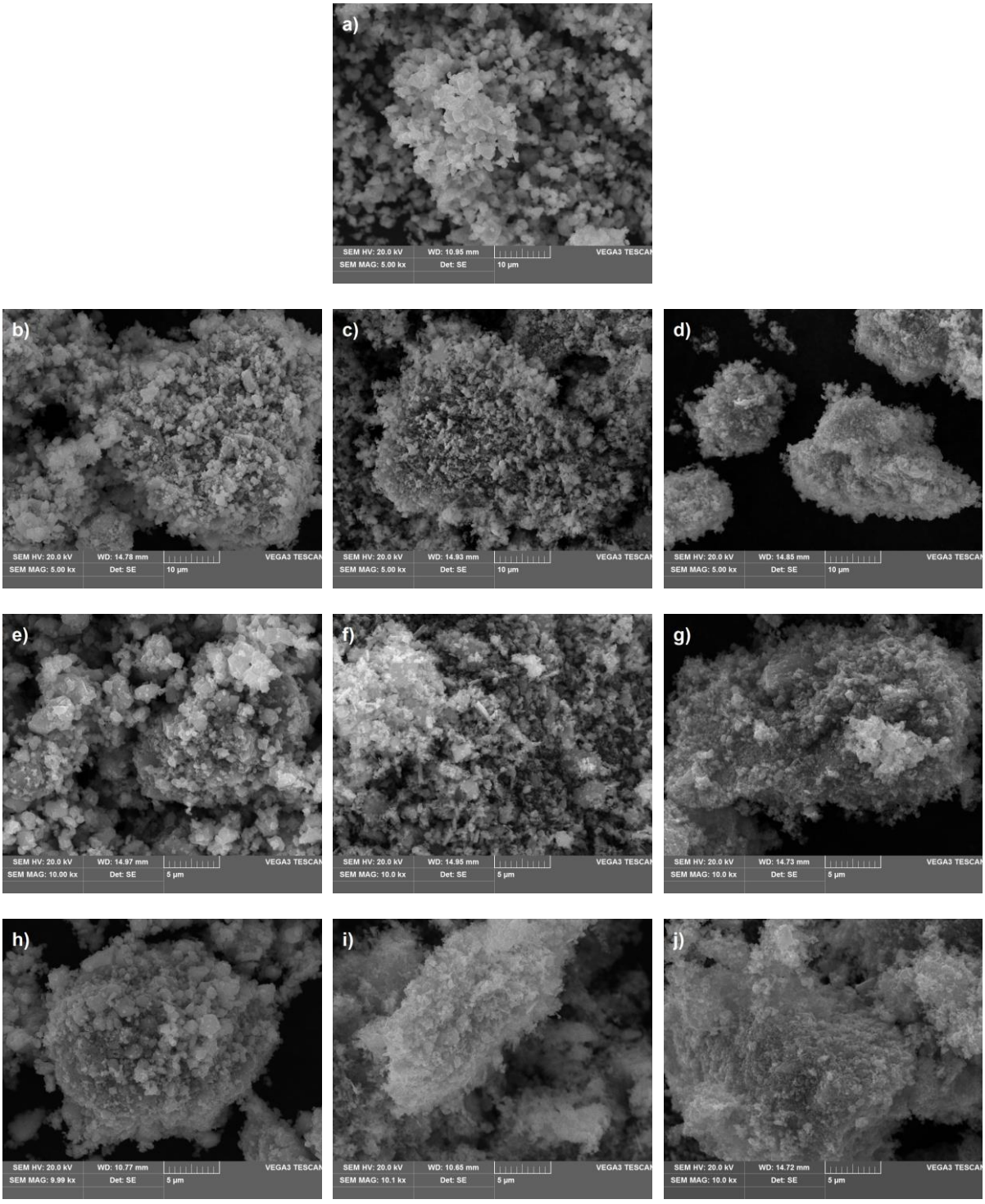

Figure 15: SEM-pictures of LTO pretreated with different methods and milling times. Picture **a)** indicates the pristine sample, in the 2nd row the 60 min milled samples are depicted **b)** either dry milled, **c)** milled with EtOH or **d)** with H_2O and a Surfactant. The 3rd row shows the 120 min milled samples **e)** dry milled, **f)** milled with EtOH or with **g)** H_2O and the 4th row indicates the 240 min milled samples, **h)** dry milled, **i)** milled with EtOH or with **j)** H_2O.

generally seem to be smaller when comparing with the dry milled sample and additionally the overall formation also seem to be porous and spongy with rod shaped edges.

A further reduction in the particle size can be noticed when considering the H_2O milled LTO (Figure 15 d, g, j), which might be a result of the surfactant assistant ball milling, protecting the particles from adhering together and thus permit an evenly milling procedure. Nevertheless, the water milled method also exhibits an accumulation of its fine particles, leading to porous structures too.

3.3 Particle Size Determination

Based on the suspicion that agglomerates could have built up in some samples, the particles size was determined via lasergranulometer and the gathered values were summarized in Table 1. It becomes apparent that 90 % of the particles deliver a diameter of more than 400 µm for the dry milled sample as well as for the EtOH milled sample, which confirm the suspicion that hard agglomerates had built up. However, it might be also possible, that those aggregations had been formed spontaneously, when getting in contact with air, water or during drying of the milling powder.

Table 1: Particle size of LTO (diameter of 10, 50 or 90% of the particles), determined via Lasergranulometer.

		d_{10} [µm]	d_{50} [µm]	d_{90} [µm]
LTO	0 min	0.20	2.85	436.76
	15 min	0.20	13.28	456.52
	30 min	0.16	9.36	448.62
	60 min	0.17	11.03	453.48
	120 min	0.16	9.45	449.90
	240 min	0.36	17.03	441.32
LTO / EtOH	0 min	0.21	2.81	433.57
	15 min	0.31	229.36	450.42
	30 min	0.25	2.20	429.32
	60 min	0.07	0.39	417.49
	120 min	0.18	1.30	415.90
	240 min	0.21	2.22	438.03
LTO / H_2O	0 min	0.30	1.63	3.31
	15 min	0.42	1.24	3.23
	30 min	0.35	1.13	3.15
	60 min	0.28	0.97	3.10
	120 min	0.18	0.80	2.75
	240 min	0.12	0.72	2.79
	12 h	0.12	0.68	2.41
	24 h	0.18	0.78	2.38

In accordance with the interpretation of the SEM-images, it can be seen, when comparing the d_{50} values, that the agglomerates of the dry milled sample generally consist of larger particles than those of the EtOH milled LTO, except the 15 min milled sample. As this is the only sample, where 50 % of the particles display a diameter of 229 µm, it can be assumed that this value refers to air bubbles.

As expected, the addition of the surfactant in the H_2O milled LTO, decreases its overall particle size. This is explainable by the fact, that the polyacrylate, coat the particle surface of the lithium titanate resulting in a particle separation when getting in contact with water due to its hydrophilic endgroups. Furthermore, it can be seen, that the d_{50} values of the H_2O milled samples can be further reduced when comparing with the other two methods, which complies with the studies of the SEM images. Both samples with a milling time of 12 and 24 h were additionally introduced to see, if the particle size can be further reduced, but as the particle size can be only reduced by 30 nm (Δ d_{90}) within 12 h, it can be concluded that this milling procedure comes to its physical limitation.

3.4 Cyclic Voltammetry

Figure 16 a – c indicates the Cyclic voltammograms of the dry milled LTO and the LTO - samples which were milled with either EtOH or H_2O. All the CV's were recorded with the scan rate of 0.05 mV/s and different milling times.

As can be seen in Figure 16 a, the CV curves of the dry milled LTO with the corresponding milling times exhibit reduction peaks in the range of 0.5 – 0.9 V and oxidation peaks in the range of 0.9 – 1.2 V. However, no real correlation between milling times and the peak intensity of the cyclic voltammetric curves can be observed. In contrast, the peaks of the EtOH milled sample (Figure 16 b) are more defined and thus three oxidation peaks can be detected at 0.9, 1.06 as well as 1.17 V, whereas only two reduction peaks are centered at 0.51 and 0.78 V, respectively. This do not fully reflect the results, found by Liang et al., where they detected only two anodic peaks at 0.95 V and 1.06 V and one cathodic peak at 0.7 V. Combined with the information of the insertion mechanism, suggested by Sun et al. (section 1.2), those peaks might be attributed to the phase evolution $Li_7Ti_5O_{12}$ and $Na_6LiTi_5O_{12}$, thus, the additional peaks on the oxidation (0.51 V) and reduction side (1.17 V) found in the present work might refer to a side reaction. However, this presumption requires further research. It also becomes apparent, that the oxidation peaks at 0.9 and 1.06 V intensify relative to the peak at 1.17 V, when raising the milling duration. Additionally, the capacity also starts to increase with higher milling time, on the oxidation side as well as on the reduction side, which is a strong indication for surface intercalation. Furthermore, another effect of higher milling time can be found in the peak

broadening, which might be explainable by the increase of amorphous parts as discussed in section 3.1.

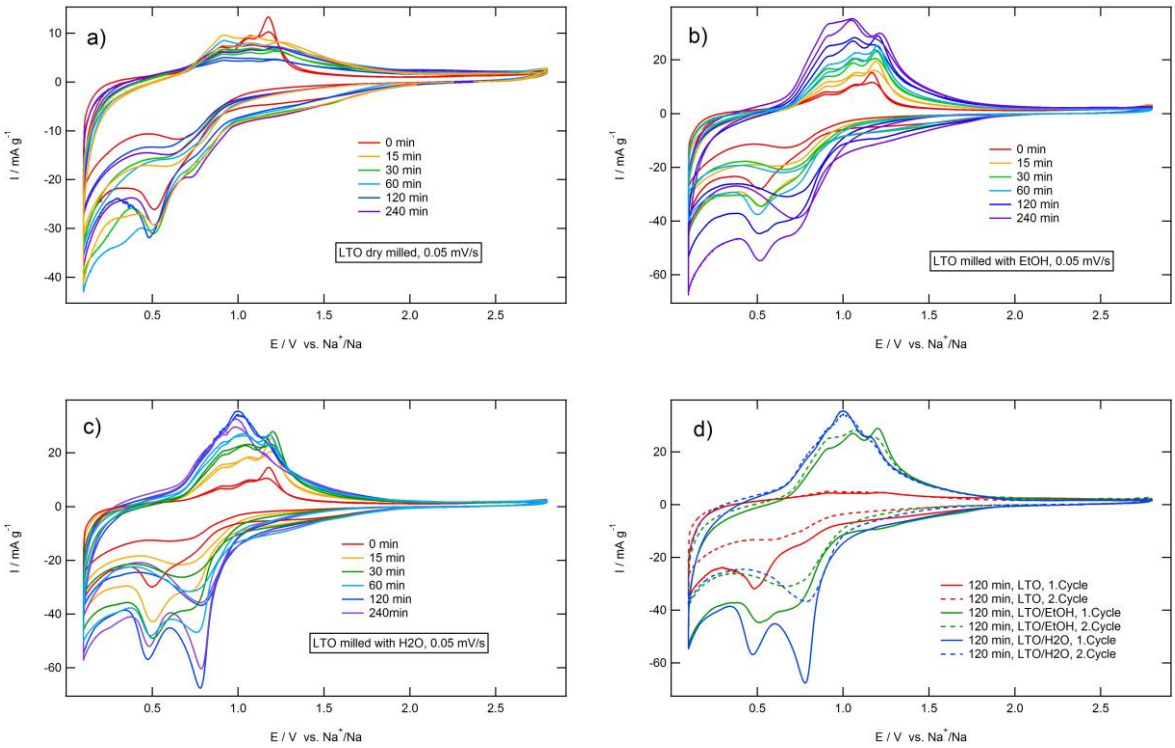

Figure 16: Cyclic voltammograms of $Li_4Ti_5O_{12}$ electrodes in 1 M $NaClO_4$/PC, by using **a)** dry milled LTO, **b)** LTO which was milled with EtOH or with **c)** H_2O and the addition of a surfactant. **d)** depicts the 120 min milled samples of all three methods.

Figure 16 c shows the cyclic voltammograms of LTO which was milled with H_2O and the addition of a surfactant. It becomes apparent, that two oxidation peaks at 0.9 and 1.06 V are merged into one broad peak when exceeding a milling time of 60 min, whereas on the cathodic side the reduction peak at about 0.7 V starts to become more intensive. Both effects might be results of phase transformation A, detected via XRD after a milling time of 30 min (section 3.1, Figure 13). Furthermore, the trend regarding the rise in capacity with higher milling time is similar to the EtOH milled sample but only until 120 min of milling. The subsequent milling step of 240 min exhibits on both sides, cathodic and anodic, a reduced capacity when comparing with the 120 min milled sample, which might be again a result of phase transformation. Since several new phases appear with 240 min (see Figure 13), which originates from a consumption of initial electroactive phases, it is not surprising that the ability to incorporate sodium ions declines. Figure 16 d displays the 120 min milled samples of all three methods with its first two cycles. It stands out that there is a tremendous difference in capacity on the cathodic as well as on the anodic side, whereas the water-milled sample exhibits the best results. The dry milled

sample, however, shows the lowest cathodic capacity, which might be a result of the larger particle size (d_{50}) as mentioned in the previous section. As a consequence, the electroactive surface decreases, which in turn lead to a reduction of accessible sites for the sodium intercalation. There is, however, almost no oxidation peak observable by considering the dry milled sample, which is an indication that an irreversible sodium storage took place. It is also worth to mention, that by comparing the first cycles with the second of all three samples, the reduction peaks at about 0.5 V disappear, whereas the alleged corresponding oxidation peaks at about 1.17 V almost remain the same, which might be attributed to an unwanted side reaction as mentioned above. This suspicion is reinforced by Figure 17 a – d, where it can be seen, that this ominous peak on the cathodic side is only present in the first cycle and the corresponding peak on the anodic side either declines in intensity or completely disappears. The other scan rates were neglected, as they only provide an overall scan of the subsequent cycles (cycle 7th – 20th).

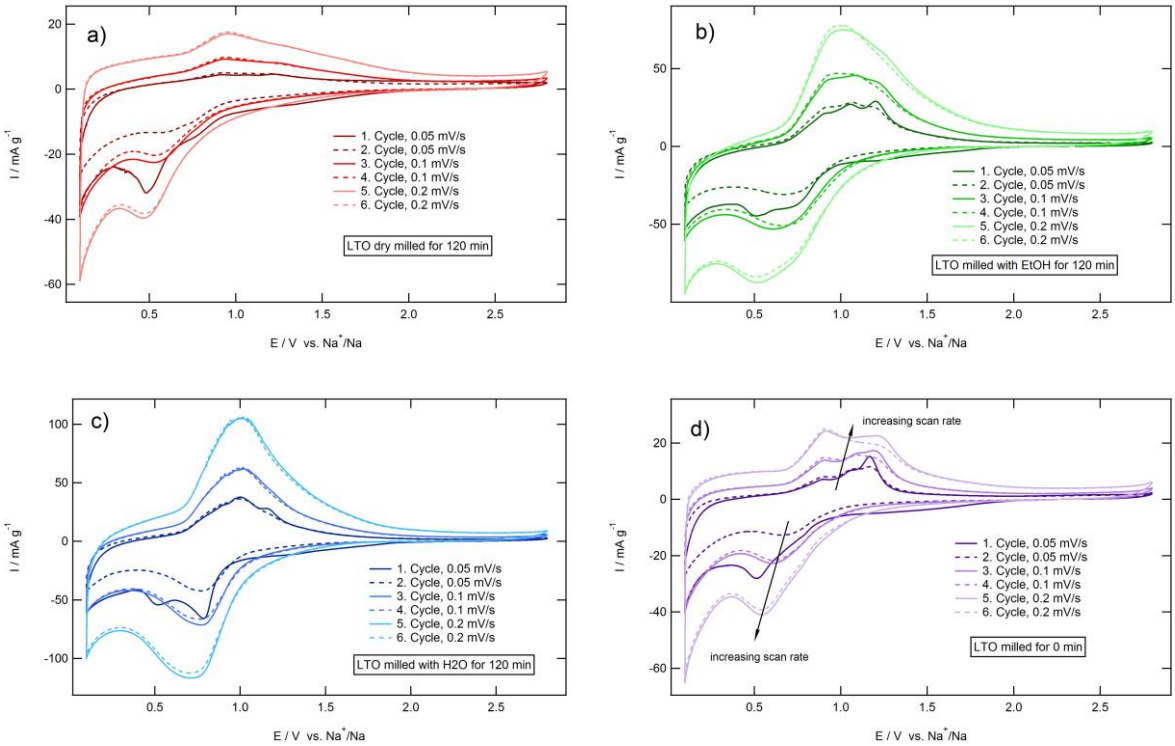

Figure 17: Cyclic voltammograms of $Li_4Ti_5O_{12}$ electrodes in 1 M $NaClO_4$/PC, by using **a)** dry milled LTO, **b)** LTO which was milled with EtOH or with **c)** H_2O and the addition of a surfactant. Additionally, **d)** indicates the unmilled LTO. All of them display the 1st – 6th cycle of the 120 min milled samples, measured with different scan rates.

3.5 Galvanostatic Cycling

The electrochemical behavior of the as-prepared LTO was further revealed by galvanostatic cycling studies. Figure 18 a – c indicate the chronopotentiometric experiments of LTO, pretreated with different methods but with the same milling time, where the cathodic (insertion) and anodic (deinsertion) capacity as well as the efficiency is plotted against the cycle number. The right column depicts the corresponding anodic capacities of each milling process.

By considering the dry milled sample in Figure 18 a it becomes apparent that there is a considerably high amount of irreversible cathodic capacity loss within the first cycles, which confirms with the results gained from cyclic voltammetry. Thereafter, the specific capacity of both, cathodic and anodic, rises the entire current step (20 mAh g^{-1} for 24 cycles). This may originate from the stepwise intercalation into the agglomerate formation of the dry milled sample, as mentioned in the previous section, meaning that after each cycle, sodium finds even more accessible site to occupy. From the illustration on the right side, it can be seen, that there is no real correlation between the milling time and the specific capacity and the maximal capacity is very low (53 mAh g^{-1}), which complies with the results found in cyclic voltammetric experiments. The EtOH milled LTO in Figure 18 b also exhibits a severe capacity fade after the first cycle, followed by a moderate decrease, which might be due to internal stress induced by the incorporation of the relatively large sodium ion. However, as illustrated on the right side the overall capacity rises continuously with higher milling time, reaching a maximum of 125 mAh g^{-1}. Finally, from the galvanostatic experiment of the H_2O milled LTO in Figure 18 c, similar cycling behavior as for the EtOH milled sample can be observed. After a tremendous capacity loss of almost 50 % within the first two cycles, the capacity moderately decreases further until it stabilizes at about 20 cycles. Nevertheless, the cathodic capacity is still higher than the anodic, leading to a reduced coulombic efficiency. The corresponding anodic capacities of all milling steps are again represented on the right side. Here it can be seen, that the overall capacity remarkably increases until the sample was milled for 60 min, where it starts to rise less steeply. After 120 min of milling time, the capacity decreases, which complies with the results gathered from cyclic voltammetry and thus again attributed to the phase transformation, mentioned in section 3.1. The highest capacity (112 mAh g^{-1}) is indeed lower than that of the EtOH milled sample, but it is, however, the highest capacity when comparing the 120 min milled samples of all methods. Therefore, it might be concluded, that if the phase transformation, which is already observable at a milling time of 60 min, did not occur, the

capacity may compete with the already stated reversible capacity of 145 mAh g^{-1} [2] from Zhao Ling et al.

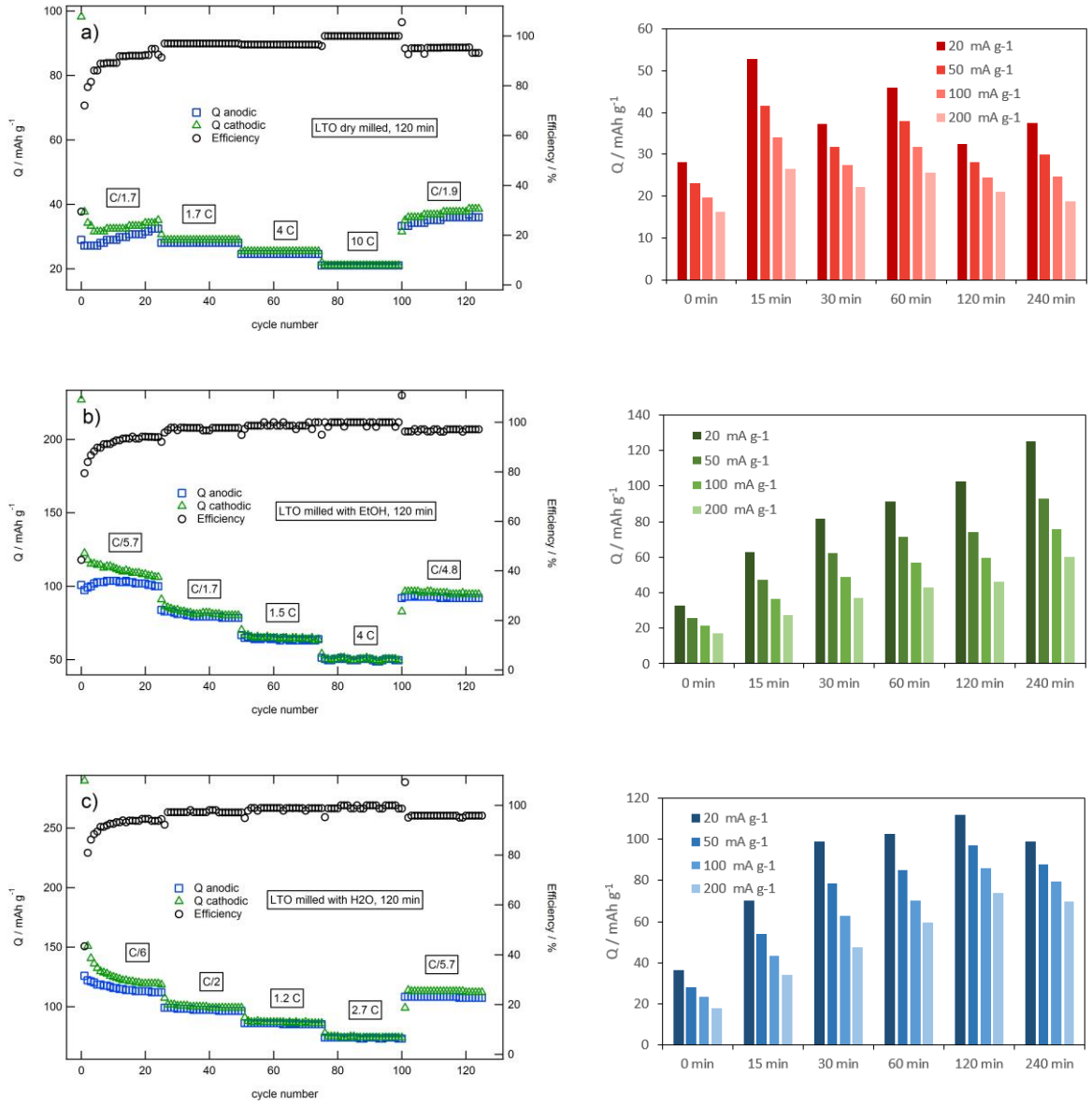

Figure 18: Galvanostatic Cycling with Potential Limitation (GCPL) of $Li_4Ti_5O_{12}$ electrodes in 1 M $NaClO_4$/PC. The LTO, was either **a)** dry milled, **b)** milled with EtOH or **c)** with H_2O and the addition of a Surfactant for 120 min. On the right side are the corresponding anodic capacities of each milling procedure.

3.6 Galvanostatic Intermittent Titration Technique

In order to determine the chemical diffusion coefficient of sodium, the chronopotentiometric method GITT was employed for the sodiation of the as-prepared LTO electrodes.

Therefore, the linear correlation between the steady state voltage and the corresponding titration step dE/dδ (Figure 19 a), as well as the linearized region between the voltage of the current pulse versus the square root of the time had to be determined in terms of equation **(5)** in section 1.3.3.1. For each linear region in Figure 19, only three values were chosen to calculate the diffusion coefficient. Figure 19 b displays the logarithmic diffusion coefficients of the sodiation into LTO (not milled), classified in part I – III and plotted against the insertion potential. As the value of the particle diameter determined via granulometer (Table 1 in section 3.3) is falsified due to the formation of agglomerates, the particle size was assumed to be 2.3 µm (d_{50}) according to the corresponding datasheet of Südchemie (the LTO manufacturer).
It can be seen, that part I, which refers to the linearized plot of y1 in Figure 19 b, exhibits the highest values of about 10^{-17} cm^2 s^{-1}. One possible explanation could be the fact that at this insertion stage, the amount of already intercalated sodium into the material is very low, so that the choice of accessible voids for additionally incoming ions is vast. As a consequence, the diffusion path for the mass transport is short, which in turn leads to a faster incorporation into the host.

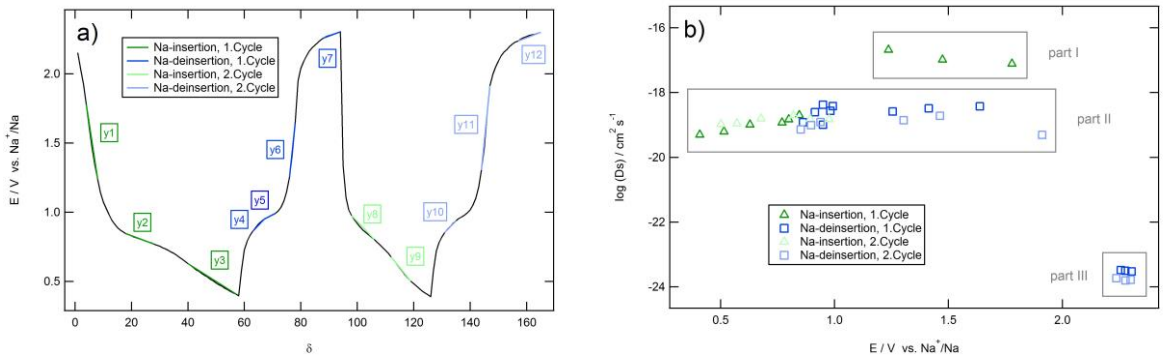

Figure 19: a) indicates the potential vs. titration step and the corresponding linear regions y1 – y12; **b)** indicates the potential dependent Diffusion coefficient (D_S) of the Na-insertion and deinsertion into/from LTO (not milled) determined via GITT-experiment, whereas part I refers to y1 in picture a, part II to y2 – y6 and y8 – y11 and part III to y7 and y11.

In contrast, the lowest Diffusion coefficients are delivered by part III, which consists of the final deinsertion stages y7 and y12 of both cycles. The reason for the seven orders of magnitude

slower diffusion, compared to part I, is ascribed to the fact that almost no sodium ion is residing the spinel structure at this particular deinsertion stage.
The remaining linear regions refer to part II, which were used to determine the average value of the sodium diffusion coefficient (log Ds = -18.8).

Since the size determination both methods (section 3.3), the dry milled as well as the EtOH milled, led to the conclusion that an aggregation took place, those samples were not taken into account. Hence, only the samples of the water milled method were used to calculate the chemical diffusion coefficient of sodium. The corresponding diagrams are displayed in Figure 27 a – f in the Appendix. Those data were again determined out of part II and gained values were summarized in Table 2. By following the milling procedure from the top down, no real correlation between the diffusion coefficient and the milling duration can be observed, which would require further studies. The chemical diffusion coefficient of sodium during the sodiation into LTO was found to be about 10^{-20} cm^2 s^{-1}, which is 5 – 8 orders (10^{-12} – 10^{-15} cm^2 s^{-1} [34]) of magnitude lower compared to that of lithium. However, sodium is much larger than lithium and thus the discrepancy is not surprising, as the size of the ion influences its transport behavior.

Table 2: Average value of the Sodium Diffusion coeffiecient calculated out of part II (defined in Figure 19) and the corresponding standard deviation.

		log (D_s) ± σ [cm^2 s^{-1}]
LTO / H_2O	0 min	-19.72 ± 0.591
	15 min	-19.70 ± 0.481
	30 min	-20.12 ± 0.558
	60 min	-20.49 ± 0.659
	120 min	-20.34 ± 0.644
	240 min	-20.21 ± 0.574

3.7 NMR

^{23}Na MAS NMR is a powerful method to prove, if an electrochemical sodiation of a material worked. Combined with the fact, that the line width depends on the amount of inserted material, it was employed to further reveal the sodium intercalation mechanism into LTO.

Figure 20 a – f displays the ^{23}Na MAS NMR spectra of sodium inserted $Li_4Ti_5O_{12}$, pretreated with different milling methods and durations, which were recorded at two different temperatures, either RT or at 100°C. It stands out, that each sample feature one peak, which is attributed to the fact that sodium resides a specific crystal position in the spinel structure. This is in agreement with the results of Sun et al. who suggested that sodium is too large to occupy the tetrahedral 8a site and thus only reside the octahedral 16c site during the sodiation of LTO. Furthermore, it can be seen that the line width does not become appreciably smaller when increasing the temperature, which implies the absence of fast ions. By comparing the three preparation methods, it becomes apparent that the samples differ in line width and in the signal to noise ratio, whereas the EtOH milled LTO (Figure 20 c, d) exhibits the lowest.

The corresponding line broadness as well as the longitudinal relaxation time T_1 of each sample, were summarized in Table 3. Following the full width at half maximum (FWHM) by raising the milling duration from 15 min to 240 min at the same temperature, a line narrowing can be observed, which is an indication that a smaller amount of sodium was inserted. This behavior does not comply with the information gained from cyclic voltammetric experiment as well as cycling studies, as those results suggested, that the insertion capacity of sodium increases with longer milling time, except the dry milled sample, which did not exhibit an observable trend. This might be explainable by an uneven sodium distribution within the inserted material, and thus the analyzed material contained less sodium. However, this assumption is not evidenced at this early stage of research and would need further investigations.
Furthermore, it can be seen that the EtOH milled samples feature, unlike the cycling studies, the lowest sodium content compared to the other methods. Another indication that the sodiation did not work satisfactorily was found in the fact, that all the other samples (dry milled and water milled) changes its color and turned blue, which originates from the partial reduction of Ti^{4+} to Ti^{3+}, whereas the EtOH milled sample remain white. One possible explanation might be a lower conductance of the sodium ions, which is induced by remaining solvent molecules. As, after the milling process, the sample was only allowed to dry in the glove box at RT, a small amount might have remained. Hence, it is not surprising that the cycling studies display better results,

as therefore casted electrodes were employed, which were dried two times at 60°C. In contrast, the water milled sample was milled prior to the annealing step, which ensures the absence of solvent molecules and thus the sodium content is reasonably high.

Surprisingly, the dry milled samples, possess the broadest line width and thus the amount of inserted sodium is also high. This result is again in conflict with the previous information, which might originate from different sodium intercalation behavior of the pure LTO and the casted electrode, which additionally contain a conductive agent as well as a binder. Furthermore, the spin-lattice relaxation time T_1 were also determined, which are in the range of 10 – 90 ms. As expected, the relaxation time is shorter when increasing the temperature.

Table 3: FWHM and T_1-values of sodiated LTO, determined via ^{23}Na MAS NMR. LTO was either dry milled or milled with a solvent (EtOH or H_2O). Each sample with a milling time of either 15 or 240 min at two different temperatures (RT or 100°C).

		FWHM [Hz]	**T_1 [s]**
LTO, 15 min	RT	10040.3	0.0514
	100°C	9432.98	0.0306
LTO, 240 min	RT	6658.94	0.0601
	100°C	6185.91	0.0334
LTO / EtOH, 15 min	RT	6021.12	n.m.
	100°C	5184.94	n.m.
LTO / EtOH, 240 min	RT	2719.12	n.m.
	100°C	2624.51	n.m.
LTO / H_2O, 15 min	RT	8422.85	0.0830
	100°C	8309.94	0.0459
LTO / H_2O, 240 min	RT	6393.43	0.0529
	100°C	5535.89	0.0153

In addition, two further samples were introduced and analyzed as can be seen in Table 4. The first one was also milled with EtOH for 3.3 h, but prior to the annealing step and the second sample was annealed only. Here, it can be seen, that the EtOH milled samples provide broader line width than the self-prepared sample in Table 3, which might be again explainable by the drying process which removes undesired solvent residues after the milling process as mentioned above.

Table 4: FWHM and T_1-values of sodiated LTO, determined via ^{23}Na MAS NMR. Additionally, measured samples, prepared by Patrick Posch and Marlena Uitz, whereas the LTO was either milled with EtOH for 3.3 h and annealed at 300°C or only annealed at 250°C. Both samples were measured at two different temperatures (RT or 100°C).

		FWHM [Hz]	***T*$_1$ [s]**
LTO / EtOH, 3.3 h	RT	7583.62	0.0708
	100°C	7150.27	0.0559
LTO, 0 min	RT	6250.00	0.0484
	100°C	5621.34	0.0186

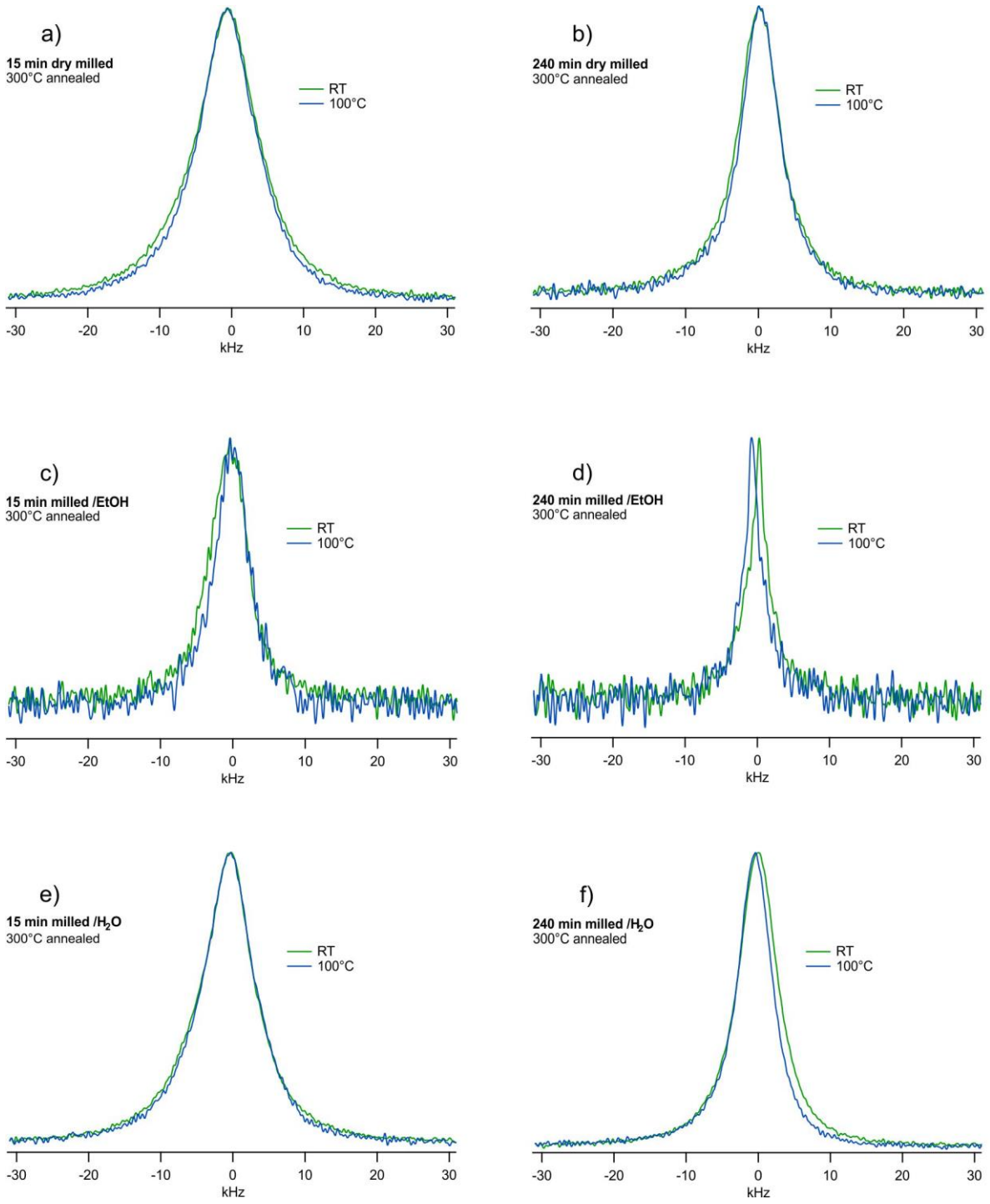

Figure 20: ^{23}Na MAS NMR spectra of Na-inserted LTO pretreated with different milling times (15 min and 240 min) and methods: either dry milled **(a, b)**, milled with EtOH **(c, d)** or H_2O and the addition of a surfactant **(e, f)**. It was recorded at different temperatures, either at RT or at 100°C.

3.8 *Ex-situ* XRD

For a better understanding of the sodium insertion mechanism into $Li_4Ti_5O_{12}$, XRD diffractograms of the sodiated sample were recorded after the de-/insertion process was stopped at specific de-/intercalation stages.

Figure 21 displays on the right side the potential limits, where the sodiation and desodiation of the water milled LTO (for 15 min) was interrupted and on the left side the corresponding X-ray diffractograms of material. It can be clearly seen, that new reflections (A, B and C) appear at an insertion potential of 0.4 V and remain the same until the anode material is fully inserted. Those reflections are attributed to the presence of a new phase (or more). Additionally, it becomes apparent, that the intensity of the reflections reffering to $Li_4Ti_5O_{12}$ declines until a full sodiation is reached at 0.2 V and afterward it increases during the deinsertion process. However, the reflections of $Li_4Ti_5O_{12}$ do not dissappear completely, which suggests that this phase coexist beside an other/others. Unfortunately, the reflections have not been identified until now due to the interferring capillary, which was used and therefore, further investigations are required.

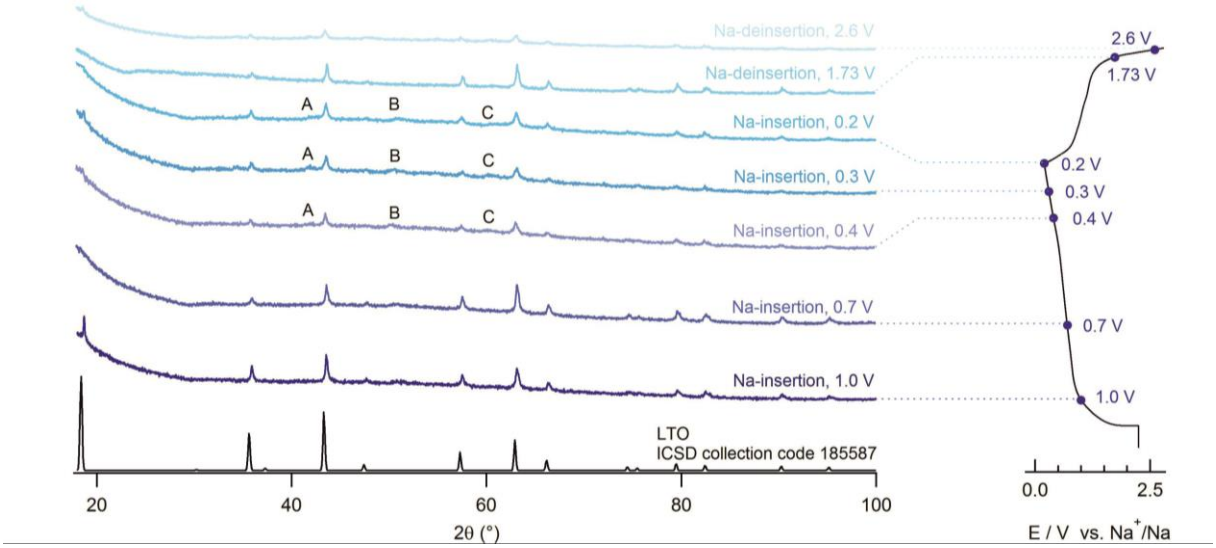

Figure 21: *Ex-situ* XRD of sodiated and desodiated LTO milled with H_2O for 15 min and the corresponding reference (black). The sodium de-/insertion was stopped at specific potential limits. Letter A indicates a lattice plane, which do not belong to the reference material.

4 Conclusion and Outlook

The aim of this work was to see, if the crystallinity or amorphicity has an impact on the sodium insertion performance of $Li_4Ti_5O_{12}$. Therefore, this spinel-type anode material was pretreated with different milling times and methods, either dry milled or milled with EtOH or H_2O and the addition of a surfactant.

The XRD analysis showed that the amorphous nature of the material generally increases when raising the milling duration. Moreover, unlike the dry milled and EtOH milled methods, the water milled LTO underwent a phase transformation, which has not been identified so far. However, all sample was found to demonstrate a correlation between the milling duration and the X-ray reflection broadness, which originates from a reduction in crystallite size. Such a trend was also observed by comparing the diffractograms of the different milling methods and thus a reduced particle size was suggested in the following order $d_{dry}>d_{EtOH}>d_{H2O}$. This was in agreement with the observation of the SEM investigations as well as the particle size determination when comparing the d_{50} values. Furthermore, the presence of hard agglomerates in the dry milled and EtOH milled sample could be detected, which might be induced by the contact with air or water during the measurement and therefore needs further research. However, the water milled samples exhibit a trend regarding a decrease of the particle size with higher milling time. Nevertheless, the particle size reduction comes to its physical limitation when reaching a d_{90} – value of 2.4 µm. The sodiation and desodiation of LTO was studied via cyclic voltammetry and galvanostatic cycling by using a Swagelok cell assembly with 1 M $NaClO_4$ in PC acting as an electrolyte. It was found out, that the anode material features a considerably high capacity fade of about 50 % or higher within the first two cycles, which could be attributed to a side reaction. Thus, after the second cycle, a reduction peak was detected at about 0.78 V and two oxidation peaks at 0.95 V and 1.06 V, resulting in an average sodium storage potential of about 0.92 V. The dry milled sample was found to mainly irreversibly intercalate sodium as the oxidation peaks are only weak identifiable. In addition, this method did not exhibit a correlation between the capacity and the milling time, which might be a result of the particle aggregation as mentioned above. However, the EtOH milled as well as the water milled sample display higher capacities with increasing milling durations, whereas the capacity of the water milled sample decreases after 120 min of milling, which could probably be explained by the phase transformation starting at milling duration of 240 min as mentioned above. Those results correlate with the cycling studies, where the H_2O milled sample reaches a

capacity of 112 mAh g^{-1}, the EtOH milled sample 102 mAh g^{-1} and the dry milled sample only 32 mAh g^{-1} when comparing the 120 min of milling time. From the GITT experiment an average chemical diffusion coefficient of sodium during the de-/sodiation of LTO was revealed to be about 10^{-20} cm^2s^{-1}. This value is, however, 5 – 8 orders of magnitude lower than that of lithium, which is due to the fact that Na^+ ions are much larger and thus influence the transport behavior to some extent. Furthermore, the NMR measurements proved that Na reside one specific crystal site, which is in agreement with the results found by Sun et al., who suggested that LTO bears sodium only at the octahedral 16c site. In contrast to the cycling studies the dry milled sample exhibits the best sodiation, which might be a result of a different insertion behavior of the pure LTO and the cast electrode. The opposite was true for the EtOH milled sample, where the sodium intercalation did not work satisfactorily, which might originate from solvent molecules that remain in the pure LTO but not in the cast electrodes which were used for the cycling experiment. Finally, the *ex-situ* X-ray diffractograms demonstrate that a new phase (or phases) starts to appear at an insertion potential of 0.4 V, but unfortunately, they are not identified so far due to the interfering capillary which was used.

It can be summarized that the solvent-based milling procedures seem to be most efficient regarding the specific capacity, which could be achieved. Thus, further investigations on this topic would make sense in order to further improve the electrochemical performance. For instance, the EtOH milled step could be also performed with the addition of a surfactant, or another solvent like Propylene carbonate could be used for the milling procedure. Furthermore, the sodiation into the pure material of the dry milled sample exhibit different results as into the casted electrode, which lead to the suspicion they might feature different insertion mechanisms. Hence, SEM images could be also taken from the cast electrode, before and after cycling. Finally, for a better identification of the reflections, which appear during the sodiation, *in-situ* XRD can be performed to reveal the insertion mechanism.

5 Bibliography

5.1 References

1. Pistoia G. *Lithium-Ion Batteries: Advances and Applications*.; 2014.

2. Zhao L, Pan H-L, Hu Y-S, Li H, Chen L-Q. Spinel lithium titanate (Li 4 Ti 5 O 12) as novel anode material for room-temperature sodium-ion battery. *Chinese Phys B*. 2012;21(2):28201.

3. Yabuuchi N, Kubota K, Dahbi M, Komaba S. Research Development on Sodium-Ion Batteries. *Chem Rev*. 2014;114:11636-11682.

4. Slater MD, Kim D, Lee E, Johnson CS. Sodium-ion batteries. *Adv Funct Mater*. 2013;23(8):947-958.

5. Kim SW, Seo DH, Ma X, Ceder G, Kang K. Electrode materials for rechargeable sodium-ion batteries: Potential alternatives to current lithium-ion batteries. *Adv Energy Mater*. 2012;2(7):710-721.

6. Brown TL, Lemay Jr. HE, Bursten BE, Murphy CJ, Woodward PM. *Chemistry - The Central Science*. 12th ed. Pearson Prentice Hall; 2012.

7. Sun Y, Zhao L, Pan H, et al. Direct atomic-scale confirmation of three-phase storage mechanism in Li4Ti5O12 anodes for room-temperature sodium-ion batteries. *Nat Commun*. 2013;4(May):1870. doi:10.1038/ncomms2878.

8. Ellis BL, Nazar LF. Sodium and sodium-ion energy storage batteries. *Curr Opin Solid State Mater Sci*. 2012;16(4):168-177. doi:10.1016/j.cossms.2012.04.002.

9. Su H, Jaffer S, Yu H. Transition metal oxides for sodium-ion batteries. *Energy Storage Mater*. 2016;5:116-131. doi:10.1016/j.ensm.2016.06.005.

10. Hong SY, Kim Y, Park Y, Choi A, Choi N-S, Lee KT. Charge carriers in rechargeable batteries: Na ions vs. Li ions. *Energy Environ Sci*. 2013;6(7):2067-2081. doi:10.1039/c3ee40811f.

11. Palomares V, Serras P, Villaluenga I, Hueso KB, Carretero-Gonzalez J, Rojo T. Na-ion batteries, recent advances and present challenges to become low cost energy storage systems. *Energy Environ Sci*. 2012;5(3):5884-5901. doi:10.1039/c2ee02781j.

12. Ponrouch a., Monti D, Boschin A, Steen B, Johansson P, Palacín MR. Non-aqueous electrolytes for sodium-ion batteries. *J Mater Chem A*. 2015;3(1):22-42. doi:10.1039/C4TA04428B.

13. Liu C, Neale ZG, Cao G. Understanding electrochemical potentials of cathode materials in rechargeable batteries. *Mater Today*. 2016;19(2):109-123. doi:10.1016/j.mattod.2015.10.009.

14. Schmidt W, Wilkening M. Diffusion-induced 7Li NMR spin-lattice relaxation of fully lithiated, mixed-conducting Li7Ti5O12. *Solid State Ionics*. 2016;287:77-82.

15. Schmidt W, Bottke P, Sternad M, Gollob P, Hennige V, Wilkening M. Small change-great effect: Steep increase of Li ion dynamics in Li4Ti5O12 at the early stages of chemical Li insertion. *Chem Mater*. 2015;27(5):1740-1750.

16. Yi T-F, Fang Z-K, Deng L, et al. Enhanced electrochemical performance of a novel Li4Ti5O12 composite as anode material for lithium-ion battery in a broad voltage window. *Ceram Int*. 2015;41(2):2336-2341.

17. Monshi A, Foroughi MR, Monshi MR. Modified Scherrer equation to estimate more accurately nano-crystallite size using XRD. *World J Nano Sci Eng*. 2012;2(3):154. doi:10.4236/wjnse.2012.23020.

18. Stanjek H, Häusler W. Basics of X-ray diffraction. *Hyperfine Interact*. 2004;154(1-4):107-119. doi:10.1023/B:HYPE.0000032028.60546.38.

19. Ermrich M, Opper D. *XRD for the Analyst - Getting Acquainted with the Principle*. 2nd ed. PANalytical GmbH; 2011.

20. Zolotoyabko E. *Basic Concepts of X-Ray Diffraction*. Wiley-VCH Verlag GmbH & Co. KGaA.; 2014.

21. Kissinger PT, Heineman WR. Cyclic voltammetry. *J Chem Educ*. 1983:1-4. doi:10.1002/9780470974001.f203017m.

22. Bard AJ, Faulkner LR. *Electrochemical Methods - Fundamentals and Applications*. 2nd ed. John Wiley & Sons, Inc.; 2001.

23. EC-Lab Software: Techniques and Applications. 2014;(August).

24. Heinze J. Cyclic Voltammetry - “Electrochemical Spectroscopy.” *Angew Chem Int Ed Engl*. 1984;23:831-847.

25. Amamiya S, Arning MD, Baur JE, et al. *Handbook of Electrochemistry*. 1st ed. (Zoski CG, ed.). Amsterdam: Elsevier; 2007.

26. Park J-K. *Principles and Applications of Lithium Secondary Batteries*. First Edit. Wiley-VCH Verlag GmbH & Co. KGaA.; 2012.

27. Bagotsky VS. *Fundamentals of Electrochemistry*. 2nd ed. Wiley - Interscience; 2006.

28. Broadhead J, Kuo HC. *Handbook of Batteries*. 3rd ed. (Linden D, Reddy TB, eds.). McGraw-Hill Companies, Inc.; 2002.

29. Galvanostatic Intermittent Titration Technique. *Metrohm Autolab Appl Note*. 2014:1-3.

30. Kim S-W, Lee S-B, Pyun S-I, et al. *Handbook of Solid State Electrochemistry I - Fundamentals, Methodologies, Application*. 1st ed. (Kharton V V., ed.). Wiley-VCH Verlag GmbH & Co. KGaA.; 2009.

31. Pyun S-I et al. *Electrochemistry of Insertion Materials for Hydrogen and Lithium*. Springer-Verlag; 2012. doi:10.1007/978-3-642-29464-8_2.

32. Weppner W. Determination of the Kinetic Parameters of Mixed-Conducting Electrodes and Application to the System Li3Sb. *J Electrochem Soc*. 1977;124(10):1569. doi:10.1149/1.2133112.

33. Zhu YJ, Wang CS. Galvanostatic Intermittent Titration Technique for Phase-Transformation Electrodes. *J Phys Chem C*. 2010;114(6):2830-2841.

34. Deng J, Lu Z, Chung CY, Xiaodong H, Wang Z, Zhou H. Electrochemical performance and kinetic behavior of lithium ion in Li4Ti5O12 thin film electrodes. *Appl Surf Sci*. 2014;314:936-941.

5.2 List of Figures

5.3 List of Tables

6 Appendix

6.1 Chemical Used

Chemical	CAS	Purchased from
$Li_4Ti_5O_{12}$ EXM T1 1037	12031 – 95 – 7	SüdChemie
Super C65	1333 – 86 – 4	TIMCAL
Kynar – Flex 2801	-	
1-Methyl-2-pyrrolidinone (NMP)	872 – 50 - 4	Sigma Aldrich
Absolute EtOH	64 – 17 – 5	Fischer Scientific UK
$NaClO_4$	7601 – 89 – 0	Sigma Aldrich
Propylene Carbonate. anhydrous 99.7 %	108 – 32 – 7	Sigma Aldrich
Dimethyl Carbonate. anhydrous ≥ 99 %	616 – 38 – 6	Sigma Aldrich
Dispex® A40	-	BASF

6.2 Thermogravimetric Analysis (TGA)

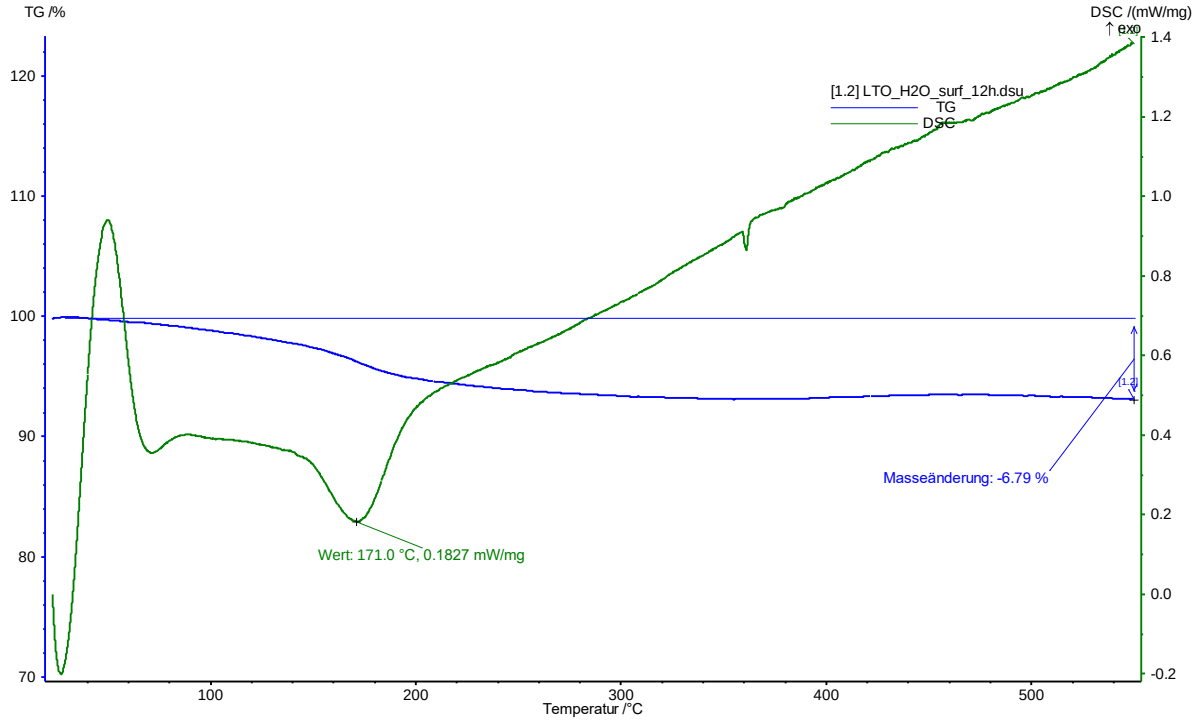

Figure 22: Thermogravimetric analysis (TGA) and Differential scanning calorimetry (DSC) of LTO milled with H_2O and the addition of a surfactant. Sample degases during the entire annealing step (from 0 – 300°C).

6.3 X-ray Diffraction

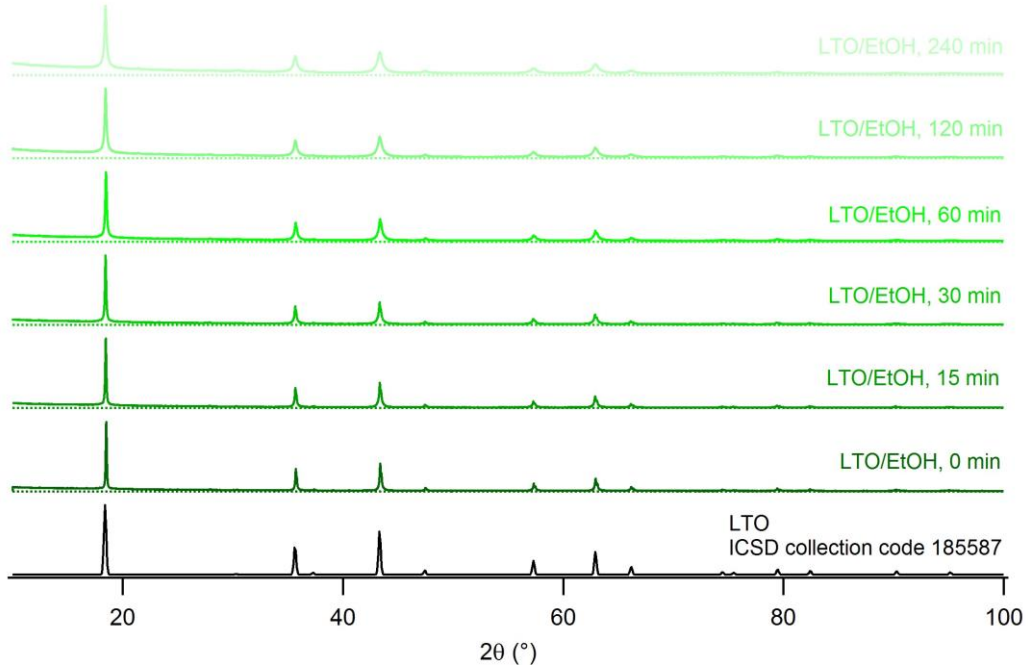

Figure 23: X-ray diffractogram of LTO which was milled with EtOH at different milling times and the corresponding reference (black).

6.4 Galvanostatic Cycling with Potential Limitation

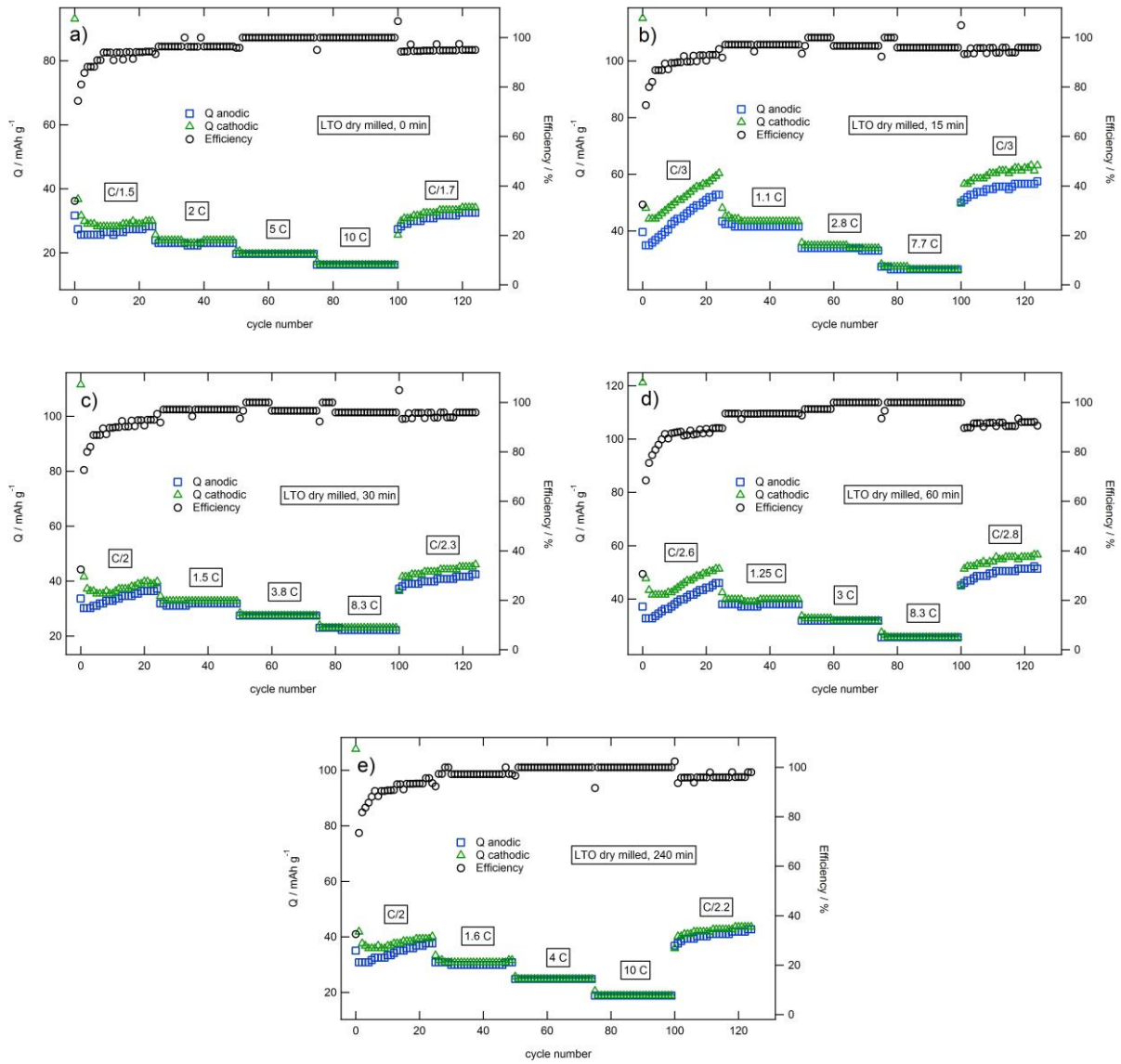

Figure 24: Galvanostatic Cycling experiment of LTO, where the capacity (anodic and cathodic) and the efficiency are plotted against the cycle number. LTO was dry milled for **a)** 0 min. **b)** 15 min. **c)** 30 min. **d)** 60 min and **e)** 240 min.

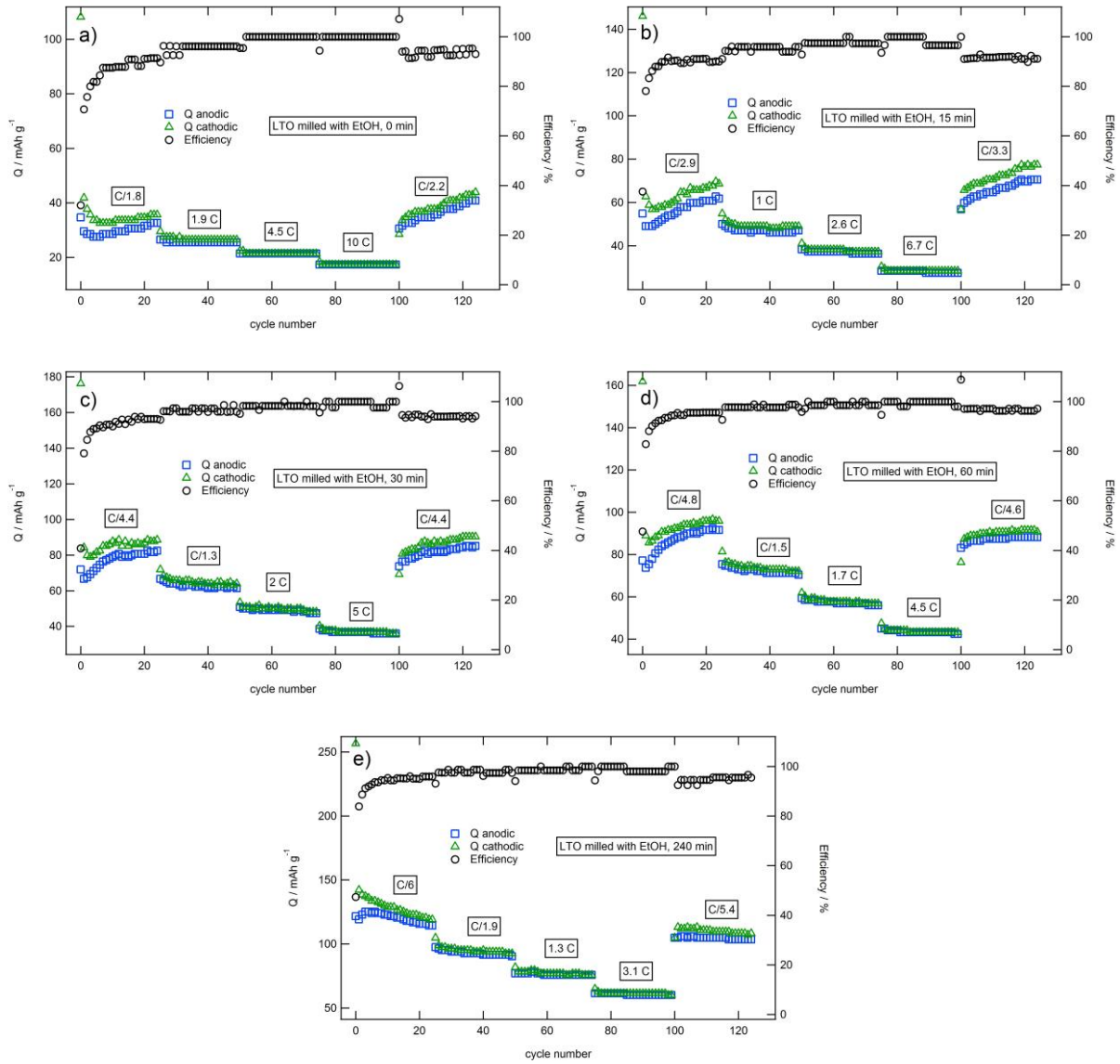

Figure 25: Galvanostatic Cycling experiment of LTO, where the capacity (anodic and cathodic) and the efficiency are plotted against the cycle number. LTO was milled with EtOH for **a)** 0 min. **b)** 15 min. **c)** 30 min. **d)** 60 min and **e)** 240 min.

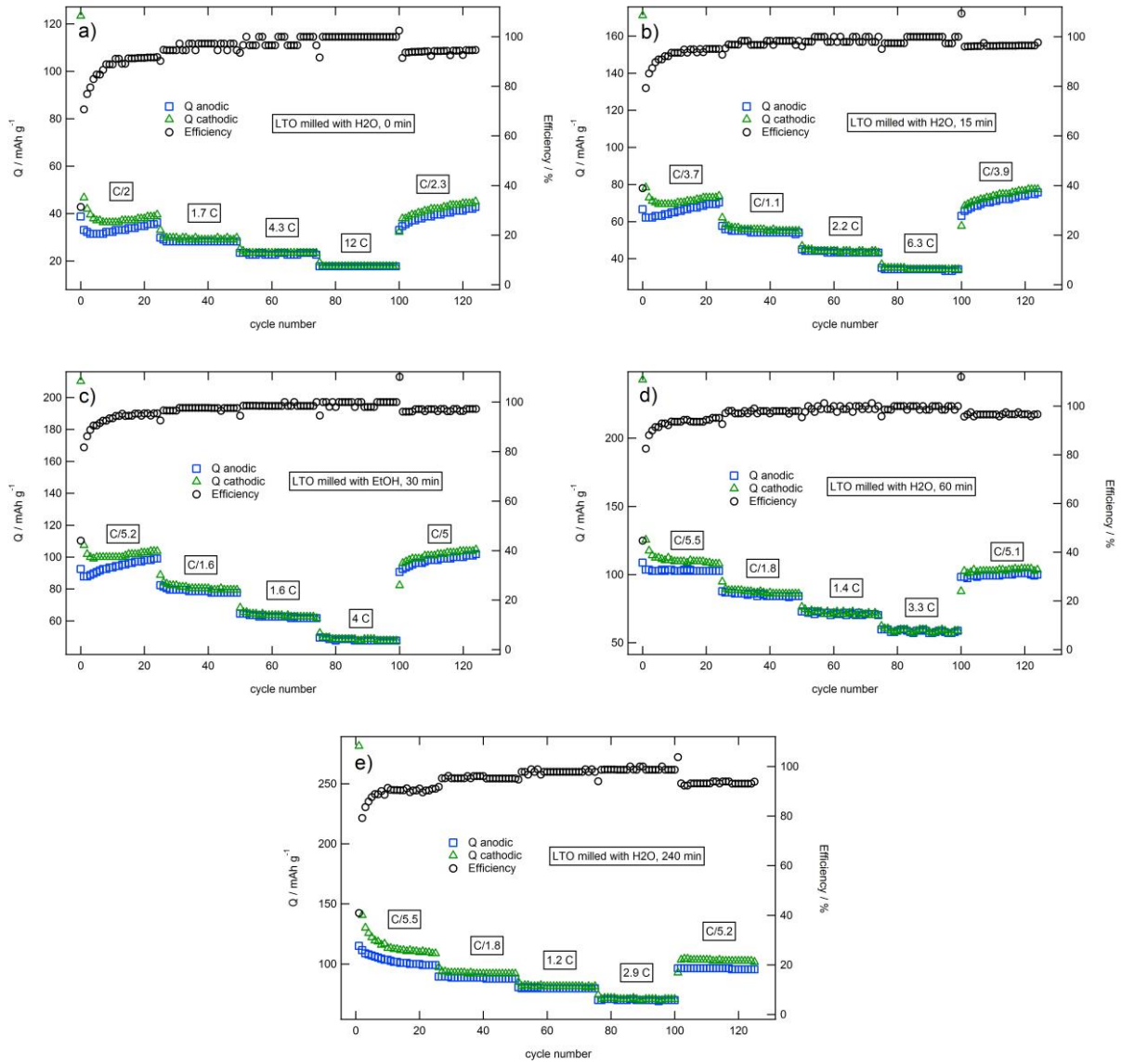

Figure 26: Galvanostatic Cycling experiment of LTO, where the capacity (anodic and cathodic) and the efficiency are plotted against the cycle number. LTO was milled with H_2O and the addition of a Surfactant for **a)** 0 min. **b)** 15 min. **c)** 30 min. **d)** 60 min and **e)** 240 min.

6.5 Galvanostatic Intermittent Titration Technique

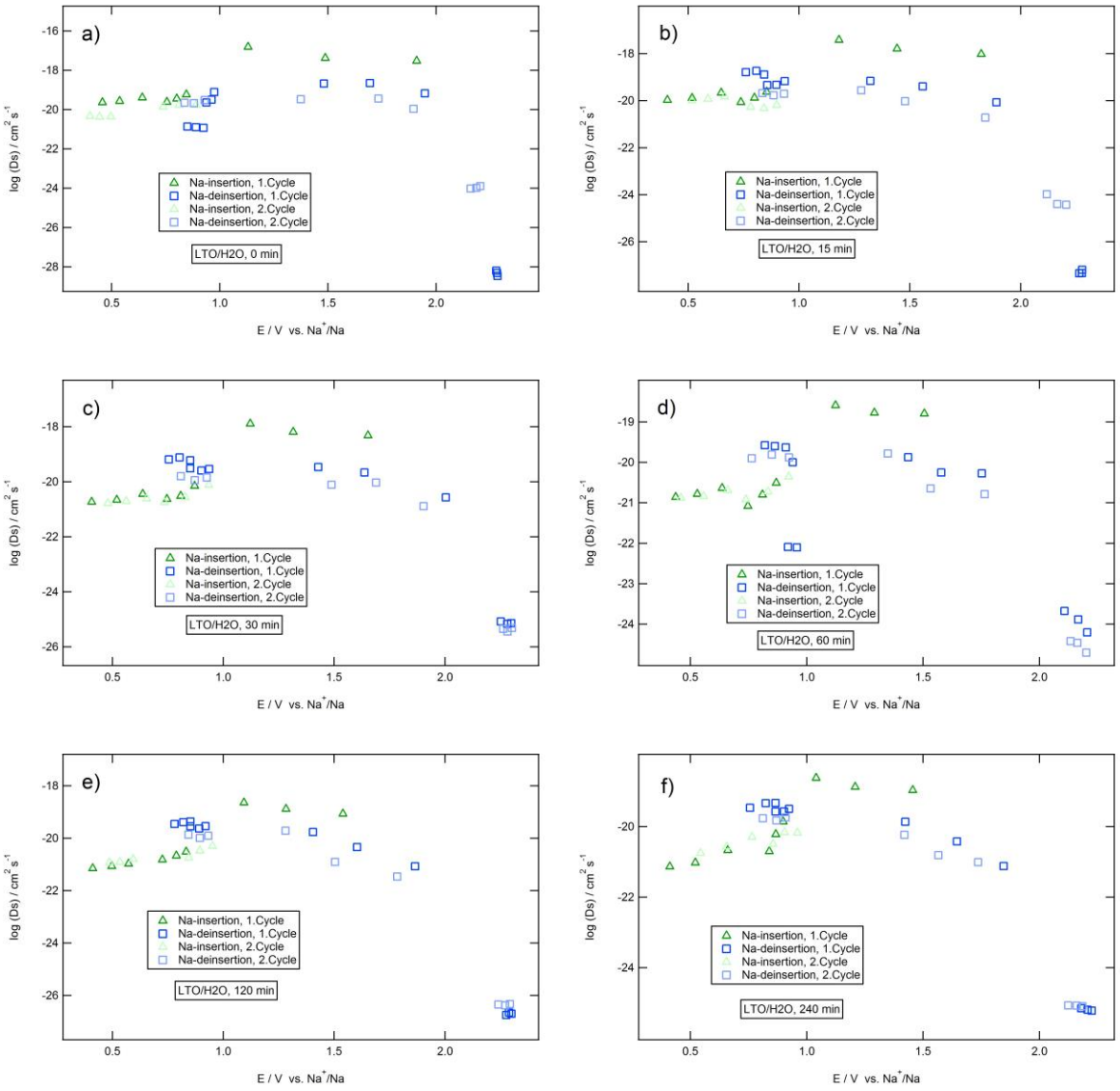

Figure 27: Diffusion coefficient of Sodium plotted vs. its insertion/deinsertion potential of LTO milled with H_2O for **a)** 0 min, **b)** 15 min, **c)** 30 min, **d)** 60 min, **e)** 120 min and **f)** 240 min.

6.6 NMR-measurements

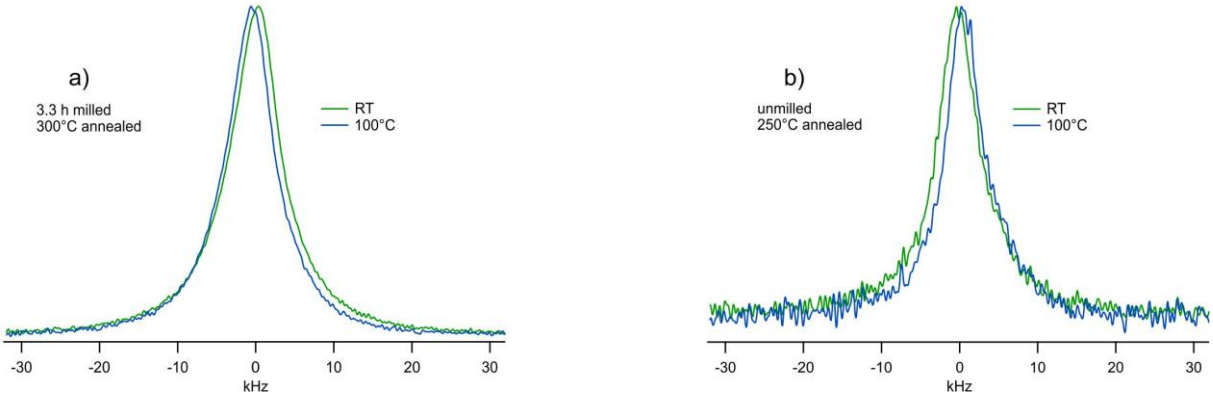

Figure 28: ^{23}Na MAS NMR of Na-inserted LTO either milled for 3.3 h and annealed at 300°C **a)** or unmilled and annealed at 250°C **b)**. It was recorded at different temperatures, either at RT or at 100°C.